Characterization of injection and confinement improvement through impurity induced profile modifications on the Wendelstein 7-X stellarator

Cite as: Phys. Plasmas **28**, 082506 (2021); https://doi.org/10.1063/5.0047274
Submitted: 18 February 2021 • Accepted: 25 June 2021 • Published Online: 10 August 2021

R. Lunsford, C. Killer, A. Nagy, et al.

Physics of Plasmas ARTICLE scitation.org/journal/php

Characterization of injection and confinement improvement through impurity induced profile modifications on the Wendelstein 7-X stellarator

Cite as: Phys. Plasmas **28**, 082506 (2021); doi: 10.1063/5.0047274
Submitted: 18 February 2021 · Accepted: 25 June 2021 ·
Published Online: 10 August 2021

R. Lunsford,[1,a),b)] C. Killer,[2] A. Nagy,[1] D. A. Gates,[1] T. Klinger,[2] A. Dinklage,[2] G. Satheeswaran,[3] G. Kocsis,[4] S. A. Lazerson,[2] F. Nespoli,[1] N. A. Pablant,[1] A. von Stechow,[2] A. Alonso,[5] T. Andreeva,[2] M. Beurskens,[2] C. Biedermann,[2] S. Brezinsek,[3] K. J. Brunner,[2] B. Buttenschön,[2] D. Carralero,[5] G. Cseh,[4] P. Drewelow,[2] F. Effenberg,[1] T. Estrada,[5] O. P. Ford,[2] O. Grulke,[2] U. Hergenhahn,[2,c)] U. Höfel,[2] J. Knauer,[2] M. Krause,[2] M. Krychowiak,[2] S. Kwak,[2] A. Langenberg,[2] U. Neuner,[2] D. Nicolai,[3] A. Pavone,[2] A. Puig Sitjes,[2] K. Rahbarnia,[2] J. Schilling,[2] J. Svensson,[2] T. Szepesi,[4] H. Thomsen,[2] T. Wauters,[3] T. Windisch,[2] V. Winters,[2] D. Zhang,[2] L. Zsuga,[4] and W7-X team[2,d)]

AFFILIATIONS

[1]Princeton Plasma Physics Laboratory, Princeton, New Jersey 08540, USA
[2]Max-Planck-Institut für Plasmaphysik, Greifswald 17491, Germany
[3]Forschungszentrum Jülich, IEK-4 Plasmaphysik, Jülich 52428, Germany
[4]Center for Energy Research, Budapest 1121, Hungary
[5]Fusion National Laboratory, CIEMAT, Madrid 28040, Spain

Note: This paper is part of the Special Collection: Papers from the 62nd Annual Meeting of the APS Division of Plasma Physics.
Note: Paper JI1 6, Bull. Am. Phys. Soc. **65** (2020).
[a)]Invited speaker.
[b)]**Author to whom correspondence should be addressed:** rlunsfor@pppl.gov
[c)]**Currently at:** Fritz-Haber-Institut der Max-Planck-Gesellschaft, Faradayweg 4-6, 14195 Berlin, Germany.
[d)]See the author list for the Wendelstein 7-X Team: Klinger *et al.*, Nucl. Fusion **59**, 112004 (2019).

ABSTRACT

Pulsed injections of boron carbide granules into Wendelstein 7-X stellarator (W7-X) plasmas transiently increase the plasma stored energy and core ion temperatures above the reference W7-X experimental programs by up to 30%. In a series of 4 MW electron cyclotron resonance heating experiments, the PPPL Probe Mounted Powder Injector provided 50 ms bursts of 100 μm granules every 350 ms at estimated quantities ranging from approximately 1 mg/pulse to over 30 mg/pulse. For each injection, the stored energy was observed to initially drop and the radiated power transiently increased, while the radial electron density profile rose at the edge as material was assimilated. Once the injected boron carbide was fully absorbed, the density rise transitioned to the core while the stored energy increased above the previous baseline level by an amount linearly correlated with the injection quantity. During the injection, the ion temperature gradient steepened with peak core ion temperatures observed to increase from a nominal 1.7 keV to over 2.6 keV for the largest injection amounts. Enhanced performance is accompanied by a reversal of the radial electric field at $\rho < 0.3$, indicating that the core transport has switched to the ion root. These observations are suggestive of a change in transport and provide further evidence that externally induced profile modifications provide a possible path to enhanced W7-X performance metrics.

I. INTRODUCTION

As fusion research transitions to long pulse devices with the goal of achieving steady state operation, both the methods of providing excellent first wall conditions and maintaining their status throughout the duration of the discharge will need to be augmented. For example, a consequence of "always on" superconducting magnets, such as those on W7-X,[1] EAST,[2] KSTAR,[3] LHD,[4] and WEST,[5] is that premium wall conditions cannot be restored by between discharge volume breakdowns. This commonly employed method, termed "glow discharge cleaning" (GDC),[6] is prevented by the shaped magnetic field.[7] By the

same token, depositional volume breakdown coating methods, such as boronization,[8] cannot be employed while the magnetic field is energized and, thus, requires a cessation of operations.[9] Given a desire to extend magnetic coil lifetime by minimizing current cycling events, it would be programmatically advantageous to develop alternate methods to modify wall conditions or getter rising hydrogen levels within standard operational conditions.

The injection of milligram quantities of low-Z particulate impurities through the use of an Impurity Powder Dropper (IPD)[10] has resulted in discharge improvements in a number of the world's leading fusion research devices. The introduction of lithium and/or boron powder into NSTX,[11] EAST,[12,13] and KSTAR[14] has led to the mitigation or elimination of Edge Localized Modes (ELMs), while boron pulses have led to an increase in confined electron and ion temperatures in LHD.[15] Improvements to overall discharge performance have also been observed on AUG in response to the injection of boron nitride.[16] In addition, the application of particulate based conditioning methods has been shown to beneficially alter the plasma material interface on DIII-D,[17] NSTX-U,[18] EAST,[19] ASDEX,[20] and most recently LHD. In these instances, the gravitational introduction of aerosolized powders, either Li, B, or BN, has been observed to have lasting (inter-discharge) effects similar to traditional wall conditioning methods.[21–23]

Given programmatic constraints, a full powder dropper installation on the Wendelstein 7-X stellarator (W7-X) was deemed temporarily impractical, and as such an alternate technology was required. A vacuum compatible periodic particle source termed the Probe Mounted Particle Injector (PMPI)[24] was developed and installed on the W7-X Multi-Purpose Manipulator (MPM)[25] probe allowing direct injection of impurities. The initial objectives of the PMPI experiments were to assess the ability of a single injector to effectively distribute the conditioning material within a stellarator geometry and, if possible, to determine whether a particulate injection system had a beneficial effect upon W7-X wall conditions. While the results of the experiments vis-a-vis improved conditioning were inconclusive, important information was observed about impurity entrainment and distribution throughout the vessel. In addition, these periodic pulsed injections were also observed to generate an unexpected transient performance boost.

In this paper, we outline the operational envelope of the PMPI and describe the first experiment undertaken with this new actuator. This includes observations of full toroidal transport of the injected material and a discussion of the supplemental calibration utilized to better characterize the quantity of the injected material. After this, we classify plasma responses to the impurity injections and conclude with a discussion detailing how those plasma modifications lead to the observed beneficial effects on overall plasma performance.

II. EXPERIMENTAL APPARATUS

Due to program requirements for mainline diagnostic commissioning prior to the most recent Operational Period of W7-X (OP1.2), it was determined that it would not be practical to install a fully integrated Impurity Powder Dropper (IPD) as was done on other devices. The arrived upon solution was to create a modified powder injector, which would allow initial experiments to be performed utilizing a temporary installation on the W7-X Multi-Purpose Manipulator[25] probe arm. The primary impetus behind the design and implementation of the PMPI was to facilitate rapid deployment of a particulate impurity source, thus allowing a characterization of the behavior of injected impurities within the W7-X topology prior to the extended programmatic upgrade between the preliminary commissioning phase of W7-X (OP1) and the latter initial research phase (OP2). The focus of these initial injection experiments was to determine the ability of a single source impurity actuator to transport the injected material throughout the vessel while assessing the stability of the discharge to the repeated introduction of a solid material. These results would then provide insight into the ability of a full IPD system to effectively operate within the constraints of a stellarator operational space.

A. The PPPL Probe Mounted Particle Injector (PMPI)

The PPPL PMPI was custom designed to provide a portion of the functionality of the PPPL Impurity Powder Dropper (IPD) system deployed on AUG,[20] EAST,[19] and DIII-D[17] within the cylindrical operational envelope of the MPM (120 mm diameter × 150 mm length). To accomplish this, the PMPI is designed with a single impurity hopper/feeder pair as shown in Fig. 1 as opposed to four feeders found in the standard IPD. A cylindrical column and funnel, comprising an 80 cm^3 volume, maintain the powder inventory. The feeder tray, located 2 mm below the bottom of the funnel, is vibrated at resonance, and this movement conveys powder down the tray toward the impeller wheel. As the major change between the operational methodology of the IPD and PMPI is the need to provide for horizontal rather than gravitational injection, a piezoelectric rotary motor specifically designed for operation in high field environments was coupled to a vertically oriented paddle wheel. The eight 35 mm long vacuum compatible thermoplastic polyether-ether-keytone (PEEK) blades attached to the central hub are machined to be slightly longer than the distance from the wheel hub to the bottom of the feed tray. During rotation, the paddles flex slightly when coming in contact with the aluminum tray scraping powder along the tray and bringing it forward. As each paddle passes the vertical axis, the flexure energy is released providing the majority of the 0.5 m/s injection velocity. The powder is projected up and forward out of the feeder tray as shown in panel (a) of Fig. 2. The quantity of powder delivered is determined by the depth of powder in the tray and can be roughly controlled by altering the excitation amplitude of the sinusoidal signal sent to the piezoelectric crystals connected to the feeder tray. At normal operation, this provides a pulsed injection every 350 ms. Laboratory tests in atmosphere have shown a maximum horizontal throw of 25 cm with the majority of the powder delivered within the range of 12 to 18 cm.[24] The need for a compact mechanical method of horizontal introduction was the primary driving force behind the actuator design and is responsible for the pulsed nature of injections from the PMPI as opposed to the more continuous flow observed during IPD operations. The entirety of the PMPI assembly is enclosed within a protective graphite covering into which a 13 × 20 mm^2 rectangular hole has been machined on the front to allow for powder injection. For these experiments, the PMPI was filled with 80 ml of loose packed granular boron carbide powder for a total inventory of approximately 100 g.

To deliver the boron carbide payload to the discharge, the PMPI is mounted to the head of the W7-X Multi-Purpose Manipulator and relayed past the vacuum boundary into the main chamber. The MPM is designed as a unique multi-user platform for plasma edge investigations and facilitates a variety of measurements through rapid replacement of diagnostic heads without the need to disrupt the W7-X main chamber vacuum conditions. For these experiments, the MPM moves

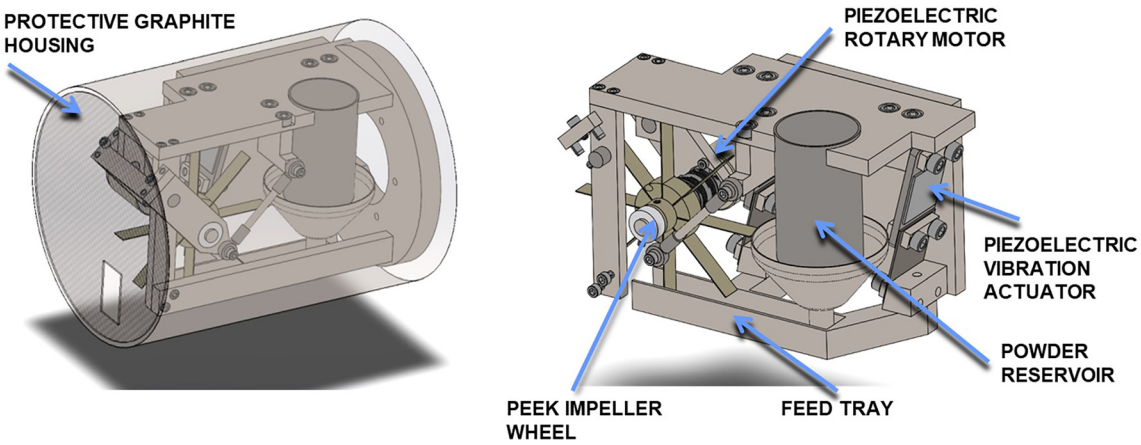

FIG. 1. Assembly drawing view of PPPL Probe Mounted Particle Injector. The right hand image points out the primary components of the injector. Powder is fed from the reservoir down into the feed tray. The tray is oscillated at resonance by the piezoelectric vibration actuator, which conveys the material from the rear to the front of the PMPI. Once the powder is driven into the discharge by a rotating impeller wheel being driven at 0.35 Hz by the piezoelectric rotary motor such that the injection frequency is 2.8 Hz. The left image shows the protective graphite housing, which isolates the interior workings from the surrounding discharge except for a small rectangular opening found at roughly the 6 o'clock position on the font face, which allows powder injection.

the PMPI probe head past the gate valves and cryostat to a parking position in line with the outer main chamber wall. During experiments, the probe was moved to locations up to 15 cm past the inner wall, a position which, based on measured Scrape Off Layer (SOL) profiles,[26] left it external to the discharge by amounts ranging from 20 cm at the furthest to 5 cm at the closest. These standoff distances allowed the probe extended dwell time at this location without substantial heat buildup on the probe's graphite shield. We note that at the shorter distances, heating of the protective carbon shell was observed during the course of the 7 s plasma exposure, although measurements on the onboard thermocouple showed the PMPI temperature to still be well within operational range.

1. Choice of Incident Injection Media

The coating of interior plasma facing surfaces is an effective way to control hydrogenic recycling and reduce impurity influx. To minimize the impact of the sputtered coating material on the effective ion charge of the plasma, low atomic number species are often selected as materials of choice for injection. Examples include lithium, boron, and silicon delivered through evaporative coating, volume glow discharge depositional coating, and plasma assisted coating. The standard version of the IPD has been successfully tested with Li, B, BN, B_4C, C, SiC, and Sn. During wall conditioning experiments on other devices, the standard gravitationally fed IPD is nominally loaded with a subset of lithium, pure boron powder, or boron nitride as the needs of the host scientific program dictate. Lithium was not a preferred option for these initial tests on W7-X, and so, the choice of the injection material was narrowed to a boron containing compound.

Previous experiments have shown that the concomitant nitrogen introduced with BN behaves in a similar manner as injected nitrogen gas and sharply raise the radiative fraction of the discharge. As such, it places a more stringent limit on the amount of material that can be

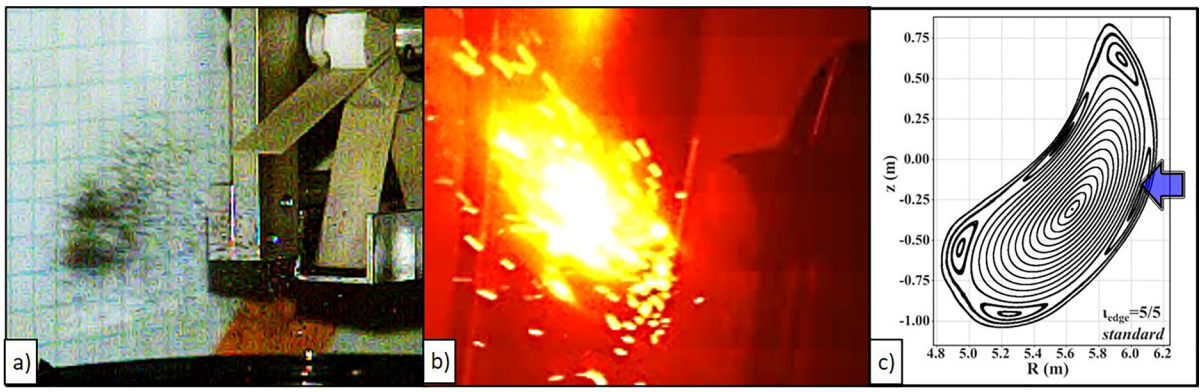

FIG. 2. Images of powder injection. Panel (a) shows the cloud of boron carbide particulates as they exit the feeder tray of the PMPI. Panel (b) is a false color image of a powder injection event during W7-X experimental program 20180927-47. The PMPI with its protective carbon cover can be seen as the cylindrical object on the right, illuminated by the ablating B_4C as it comes in contact with the edge of the discharge. A Poincare map is shown in panel (c) with the blue arrow showing the location of the powder injection and the tip of the arrow indicative of the approximate initial edge penetration depth.

injected prior to the onset of a radiative discharge collapse. Pure boron powder does not lead to these sharp increases in plasma radiation and as such would have been the preferred choice of an injection material. However, it has been observed that under certain conditions, the boron powder load can tend to aggregate and form clumps, which inhibit the material flow and, thus, optimal performance within a standard IPD. When the system is mounted external to the vacuum vessel, identifying and resolving this issue are minor inconvenience; however, as the PMPI is internal to the vacuum boundary, such clumping could not be easily remedied. It was determined, therefor, that boron carbide would be a better choice of injection medium as the carbon within the crystalline lattice acts in a manner similar to a graphite lubricant and keeps the particulate flow clump free. The material utilized here is of the same stock as was previously analyzed in Fig. 4 of Ref. 27 and injected into DIII-D[28] for multi-species granule experiments and was, thus, deemed suitable for injection into a research plasma environment.

B. Wendelstein 7-X

Wendelstein 7-X is a fivefold symmetric stellarator of major radius 5.5 m and minor radius 0.5 m with an interior plasma volume of about 30 m^3. The magnetic flux surfaces are generated by a set of external planar and non-planar superconducting coils, and the field geometry has been drift optimized to minimize neoclassical transport losses while maintaining MHD stability.[29,30] Primary plasma heating through electron cyclotron resonance heating (ECRH) supports moderate densities (relevant to this paper $< \sim 0.5 \times 10^{20}$ m^{-3}) with electron temperatures Te $\sim$ 5 keV and ion temperature $T_i < 1.6$ keV in quasi-stationary discharges. In anticipation of stable high-beta operation, consistent control of first order heat loading at 10 island divertor modules has been achieved[31–33] and power and particle exhaust during the two most recent operational phases, OP1.2a and OP1.2b, are controlled through the use of this helically shaped island divertor concept.[34–36]

To provide suitable machine conditions, the inner plasma facing components (PFCs) were covered with graphite tiles while baking as well as glow discharge cleaning (GDC),[37] provided a baseline set of conditions for the experimental campaign. To maintain wall conditions, a series of short ECRH pulse trains immediately followed by pumping intervals was employed to reduce the PFC outgassing rate.[38] In addition, experiments were alternately run with hydrogen and helium working gasses to desorb first wall hydrogen content providing enhanced density control.[21,22] After three out of the thirteen experimental weeks of OP1.2b, a deposited boron coating was applied through a volume breakdown helium glow discharge doped with a 10% concentration of diborane gas (B_2H_6). The 4 h boronization discharge deposited an approximately 100 nm boron coating on the plasma facing components and was observed to reduce the normalized influx of oxygen and carbon by factors of approximately 10 and 4, respectively, indicating gettering by the boron layer.[23] These boronization conditioning discharges were run three times over the course of the experimental campaign.

1. W7-X Diagnostics

Diagnostics on the W7-X stellarator provide well resolved measurement of plasma characteristics. Electron temperature and density profiles are provided by Thomson scattering,[39,40] while the line averaged density is measured by a dispersion interferometer[41] and measurements of the plasma stored energy are derived from a compensated set of three diamagnetic loops.[42] Impurity levels within the discharge are measured by the High-Efficiency XUV Overview Spectrometer (HEXOS),[43] and divertor imaging is provided by a visible camera equipped with a Carbon III spectroscopic line filter.[44]

The overview visible camera array[45] provides images through ten ports with tangential plasma views. Camera heads at the end of a series of bellows generate observational viewing cones, which stretch through the module where the respective ports are located and terminate in a line of sight intersection with the vacuum vessel in the adjacent module as can be seen in Fig. 3. These camera views are labeled with the moniker AEQ##, with the first number denoting the module where the port is located and the second number, either "0" or "1," denoting if the view is clockwise or counterclockwise around the vessel, respectively. For example, mounted onto the AEQ31 port (purple box in figure) is the counterclockwise viewing camera in module 3, which directly observes the PMPI injection located in the middle of module 4. For odd numbered ports, the camera views the interior of the module where it is located as well as the adjacent increasing number module (i.e., AEQ11 view terminates in module 2 and the AEQ51 view terminates in module 1 as the circuit is completed). Even numbered observational ports record views clockwise from the camera origin into the decreasing module number (i.e., the AEQ50 view terminates in module 4). The need for this precise distinction comes from utilizing these images and specifically their time history to track illuminated structures as they transit the vessel as will be discussed in Sec. III A.

Ion temperature measurements as well as measurements of the radial electric field are determined by monitoring the perpendicular velocity of non-perturbing seeded argon gas utilizing the x-ray Imaging Crystal Spectrometer (XICS).[46,47] Measurements of the highly

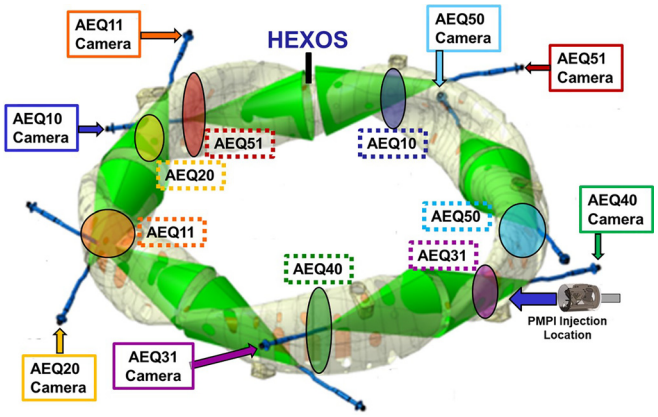

FIG. 3. Camera image location in W7-X. The locations of the high speed survey cameras are denoted by the colored boxes with attached arrows. A bellows extends from the camera port, through the cryostat and to the edge of the vacuum vessel as denoted by the associated blue cylinders. The green cones emanating from each camera location show the field of view of the respective camera, and the associated colored ovals in the above figure show the approximate location where the camera view intersects the vessel wall with the associated origin port labeled in the dashed boxes. Also denoted by a black bar is the toroidal location of the HEXOS diagnostic.

ionized Ar dopant (Ar^{16+}, Ar^{17+}) provide flow velocities from a doppler shifting of the emission lines as well as ion temperature through an analysis of the line broadened spectroscopic signal. The radial electric field can then be inferred from the radial component of the local force balance equation using the flux surface averaged perpendicular flow velocity.[48]

Finally, the Doppler Reflectometer (DR) system,[49–53] located at the AEA21 port, injects microwave radiation at a scanned frequency from 50 to 75 GHz in steps of 1 GHz every 10 ms to monitor spatio-temporal evolution of density fluctuations. Utilizing transmitted and received signals, the distance to a reflecting layer within the plasmas is recorded. A fixed probe beam angle of $\alpha = 18°$ is sensitive to density perturbations with finite perpendicular wave number such that $k_\perp \rho \sim 1$, providing a measure of the perpendicular rotation velocity. By observing the power of the back scattered signal, radially resolved density fluctuations can also be obtained. This current experimental layout of this system is described in Ref. 54. Of note, an attenuation of the fluctuation level during periods of enhanced confinement, such as after a series of fuel pellet injections,[55] has been observed to indicate a change in the nature or intensity of the turbulence structures.

III. EXPERIMENT

For these experiments, repeated pulses of 100 μm diameter B_4C granules were injected into a series of W7X discharges at varying quantities to evaluate plasma robustness to injection, gross toroidal impurity transport, and any effects on plasma performance. Over a series of seven discharges, the injection quantity was varied from approximately 1 mg/pulse to 30 mg/pulse and the location of the front face of the PMPI was varied between 20 and 5 cm from the nearest island scrape off layer. The closest point of an approach places the front of the PMPI approximately 10 cm from the last closed flux surface (LCFS). Injection frequency was maintained at 2.8 Hz throughout the experimental series as this represented the maximum angular velocity of the rotational motor and ensured the longest horizontal throw. For this injection frequency, the laboratory measured injection velocity was 0.5 m/s. Based on the duration of ablation and estimated injection velocity, we anticipated a radially injected granule to penetrate roughly 5 cm into the discharge as shown in panel) of Fig. 2. We note, however, that this injection velocity figure is only valid prior to the beginning of ablation at which point the granules become charged and respond to the electromagnetic forces present. Most specifically, the rapid influx of fast electrons responsible for ablation results in granules within the cloud becoming negatively charged and electrostatically repelling each other leading to accelerated cloud dispersal as observed in the overview camera image.

A. Gross Toroidal Impurity Transport

First order observations of toroidal impurity transport are provided by an array of high speed (100 Hz) survey cameras installed on W7-X. The array of images in Fig. 4 shows the evolution of illuminated field aligned structures resulting from an injection event. The field of view of the AEQ20 camera used here is toroidally opposite to the PMPI location. The injection occurs at 5.07 s, and the first image in the series shows the camera view before material has transited the vessel. As can be seen in the next panel, the injected material results in a series of distinct illumination bands with the peak of the injection as seen in the third panel exhibiting extended edge radiation bands. A comparison of the first and last images shows that the dissipation of the distinct edge illuminated structures occurs more quickly than the decay of overall discharge radiation. Given the visible spectral response of these cameras, the higher ionization states of the boron in the core would not be recorded by these images and as such this widespread illumination is indicative of strong poloidal mixing of the injected boron within the discharge edge.

Similar responses can be observed in all five modules in response to injection. The concurrent images from multiple camera locations at $t = 5.12$ s can be seen in the photo-array displayed in Fig. 5. The large center panel displays the image recorded by the camera installed at the AEQ31 port, which is focused on the MPM location and, thus, the PMPI injections. The injection pulse highlighted here started 50 ms prior to the images shown. Between the pulse initiation and the time of the frames displayed in these images, the material has transited throughout the vessel. A frame by frame integration of the pixel intensities within the camera images generates a time history of the injection event, and by then, correlating signal intensity rises with the camera image plane location, a rough estimation material spread can be determined. In Fig. 6, the first indications of the injected pulse come from the AEQ31 view, corresponding to a direct observation of the MPM location. Increased signal coincident with the arrival of radiative impurities is next observed by cameras associated with the

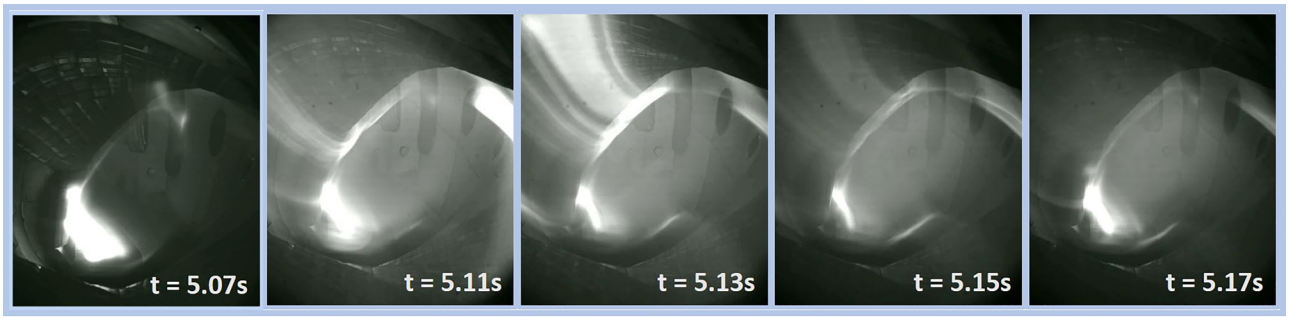

FIG. 4. Evolution of field aligned impurity structures far from the injection site. Views from the visible survey camera AEQ20, approximately toroidally opposite the injection location, show the development of illuminated bands resulting from material ablation. Material is injected at $t = 5.07$ s during W7-X experimental program 20180927-47, and propagation is evidenced by the illuminated structures in the middle three panels. Given the spectral response of the visible camera, the enhanced radiation in the final panel is most likely due to radiative boron distributed poloidally throughout the plasma edge.

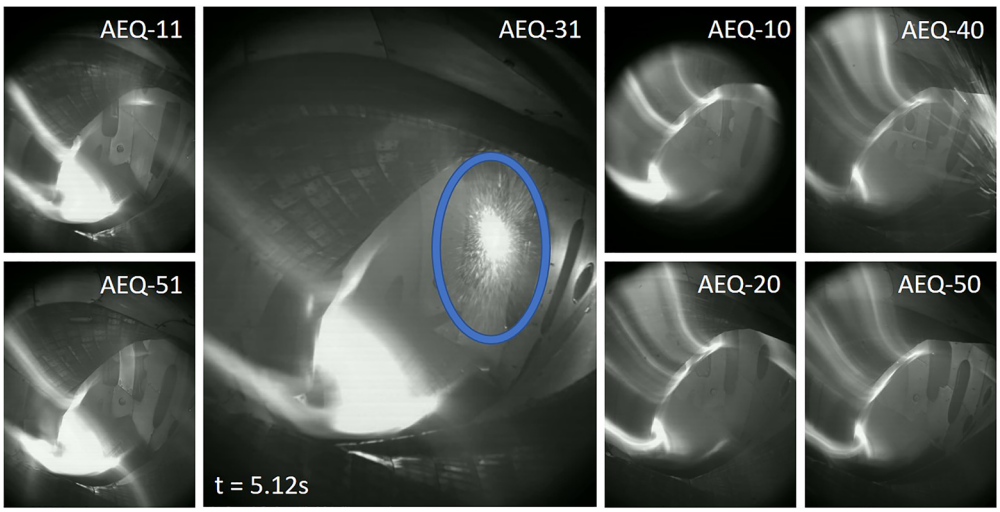

FIG. 5. The above array of images displays simultaneous views from multiple cameras providing a snapshot of impurity propagation around the internal volume during W7-X experimental program 20180927-47. The impurity pulse begins at t = 5.07 s and by the time of the images at t = 5.12 s has generated illuminated field aligned structures throughout the vessel as well as an increase in overall discharge radiation. Odd numbered panels show counterclockwise propagating views within the vessel and even numbered panels show clockwise propagating views and are inverted. The blue circle highlights the PMPI injection location in the large AEQ-31 view.

AEQ40 and AEQ50 ports, which have views directly clockwise and counterclockwise to the PMPI location, respectively. The simultaneous observation by both cameras and the further rise in all other cameras indicate that there is no dominant preferential streaming direction for the recently entrained impurities. Fitting curves to the intensities and examining the gap between peak illumination times in AEQ31 and AEQ51 camera views provide a time of flight for the pulse of approximately 15 ms, which gives an approximate toroidal entrainment velocity of 1200 m/s with an estimated error of ±400 m/s.

The *in situ* particle deposition method of wall conditioning is envisioned as supplemental to a standard boronization. With an initial conditioning volume breakdown being utilized to coat all interior surfaces of the vacuum vessel, the introduction of boron particulates into nominal W7-X discharges would provide a deposition of the injected material onto high fluence plasma surfaces, such as limiters and

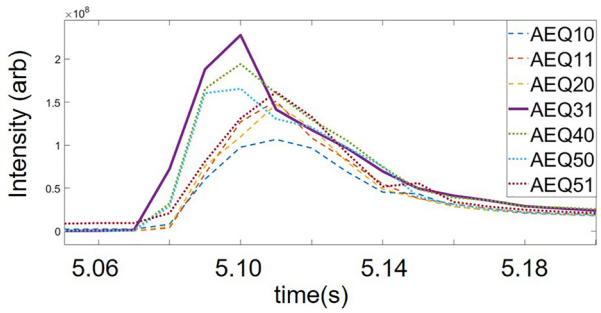

FIG. 6. Integral intensities from the visible camera array during 20180927-47 show time evolution of impurity propagation around the W7X vessel. The AEQ31 camera directly observes the injection site, which explains the leading response. The AEQ40 and AEQ50 views are directly clockwise and counterclockwise, respectively. The simultaneous rise of the later signals indicates that there is no dominant preferential direction for powder propagation.

divertors, to extend the coating lifetime and to maintain overall peak performance. Observations of the interaction between the injected material and these components were undertaken to ensure that there is strong engagement between the injected material and some of the surfaces where conditioning is required. The upper panels of Fig. 7 display Carbon III filtered images of the Module 1 upper divertor during an injection series. These images show a substantially enhanced carbon signal during the injection period. Given that the boron and carbon are injected concurrently, it is reasonable to assume that there is a substantial presence of boron also engaging with the divertor surface. With experiment 20180927–47 undertaken in the 5/5 standard configuration, a field line trace from the estimated injection location is shown in the lower panel of Fig. 7. The PMPI and the start of the material evolution is outlined in the box labeled (a) where the red line is a single field line starting at R = 6.04 m. This location represents the approximate penetration depth for a nominally injected granule as estimated by the injection velocity and ablation duration. The field line is then evolved for ∼100 m, illustrating a field-parallel pathway throughout the vacuum vessel. We note that this trace includes the module one upper divertor, also shown in Fig. 7 within a dashed box labeled (b).

The trace provides an indication where direct deposition of a material may occur; however, we note that these initial field line tracings do not account for any dispersion within the discharge or poloidal spread in the injected material. As can be seen by the presence of the bright bands in the top middle panel of Fig. 7, there is a substantial volume circulation of the injected material, which can be understood by noting that the material introduction provided by the PMPI, as seen in the large central panel of Fig. 5, is not point-like and as such we can anticipate a substantial evolution of the material throughout the vessel.

B. Quantification of injection quantities

Due to the stochastic nature of coupling between the PEEK paddles and the material within the feeder tray, as well as variances in

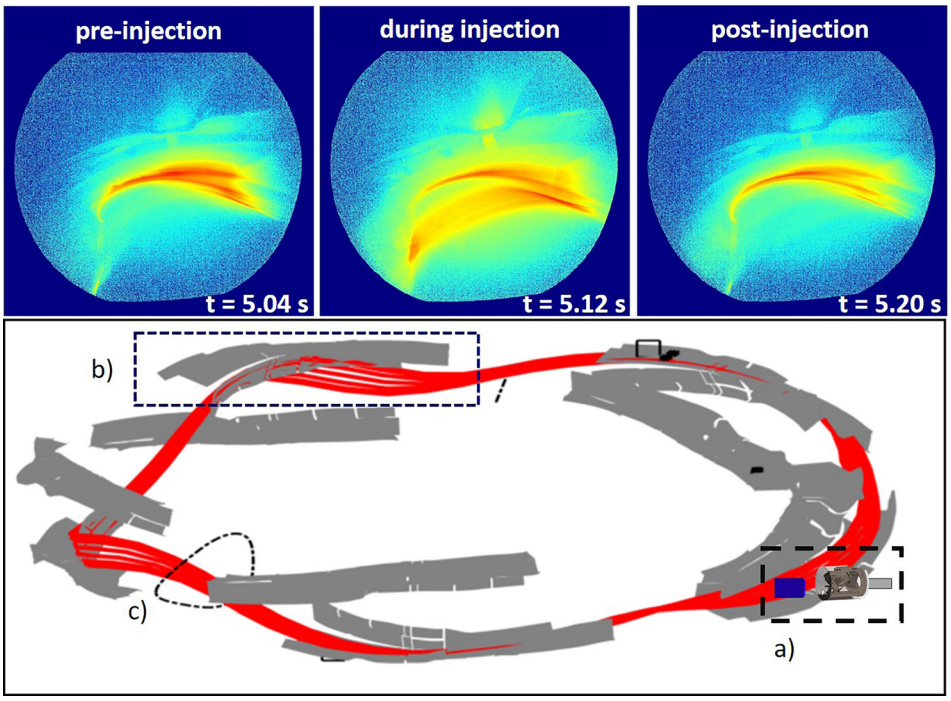

FIG. 7. Interaction of injected material with divertor surfaces. The top row of images displays carbon-III filtered imaging of the module 1 upper divertor showing enhanced interaction during an injection event within W7-X experimental program 20180927-47. The three images show the module before, during, and after the conclusion of the injection event. The lower image shows field line tracing from the injection site, labeled (a) to the module 1 upper divertor, labeled (b). The dotted outline denoted by (c) represents the plasma extent in the area between divertor modules and is representative of the AEQ camera even numbered views as seen in Fig. 5.

powder depth occurring during conveyance from the reservoir to the paddles, there is substantial discrepancy in the quantity of material disbursed by each PMPI pulse. While the injector was never intended to deliver precision quantities of material, it is nevertheless possible and appropriate to attempt to determine an approximate injection quantity per pulse for initial analysis purposes.

A calibration of the feeder flow rate was performed prior to installation on W7-X and can be found in Ref. 24. It was also determined that the average coupling efficiency between the PEEK paddle and the material contained within the tray is approximately 50%. That is, 50% of the material within the tray is projected upward and forward into the plasma, while the remaining material is captured by the lip on the carbon cap just in front of the feeder tray. This feature was designed to direct insufficiently accelerated particulates to an open area in the bottom of the protective carbon cap just underneath the PMPI structure. As an example, mass throughput calculation, we note that during the experimental program W7X20180927–07, the average throughput of the feeder tray at the voltage selected for this discharge was 6 mg/s based upon laboratory calibration. Given a paddle frequency of 2.8 Hz in conjunction with the 50% injection efficiency, this provides an estimated material injection quantity of approximately 1 mg/pulse.

These pulses are then further characterized by correlating the laboratory calibration with images of the injection events as provided by the overview video diagnostic system,[56] a representative image of which is illustrated in Fig. 2(b). Given the stochastic toroidal spread of the material, the only way to ensure that the majority of the PMPI injection was accounted for was to directly observe it at the injection point. With this in mind, the illumination provided by the fast visible camera was chosen to provide a post-facto quantification. Experimental program 20180927–07 was chosen as a reference injection discharge as the PMPI was programmed for a minimal excitation level, and thus, we believe the injection to be well characterized. The left panel of Fig. 8 displays the evolution of plasma parameters, namely, P_{ECRH}, P_{RAD}, n_e, T_e, T_i, and W_{DIA}, showing the minimal plasma response to small injections, while the right panel shows a time history of injection events. This series was generated by performing a background subtracted summation of the pixel intensities in the area around the PMPI. The video images of injection events from this experimental program are then compared to the peaks to determine which events are due to powder injection, and these are denoted in the figure by the red arrows. Peaks following injection events are integrated to determine total ablation generated illumination, and the average of the first 12 pulses was utilized to determine an empirical conversion factor between signal intensity and calibrated injection amount. The final pulse, being over a factor of 2 larger than any other injection event in this discharge and, thus, indicative of an off normal event, was not included in the average. Completing this process leads to an estimated conversion factor of 4.2×10^6 counts/gram with a standard deviation of 2.2×10^6 counts/gram. A nominally linear response of the CMOS sensor over the intensity range then allows us to utilize this conversion factor to estimate injection quantities in future discharges with larger injection amounts.

This method of post-facto calibration does not come without qualifications and limitations. In general, the illumination generated by impurities can be highly dependent upon material density as well as electron density and temperature. However, as the penetration depth of the granules prior to full ablation is on the order of 5 cm and as the camera is only sensitive to visible emissions, we assert that the images being recorded are generated at the outer edge of the discharge. Here, the profile characteristics are dominated by edge interactions and recombination and as such are fairly consistent over the course of

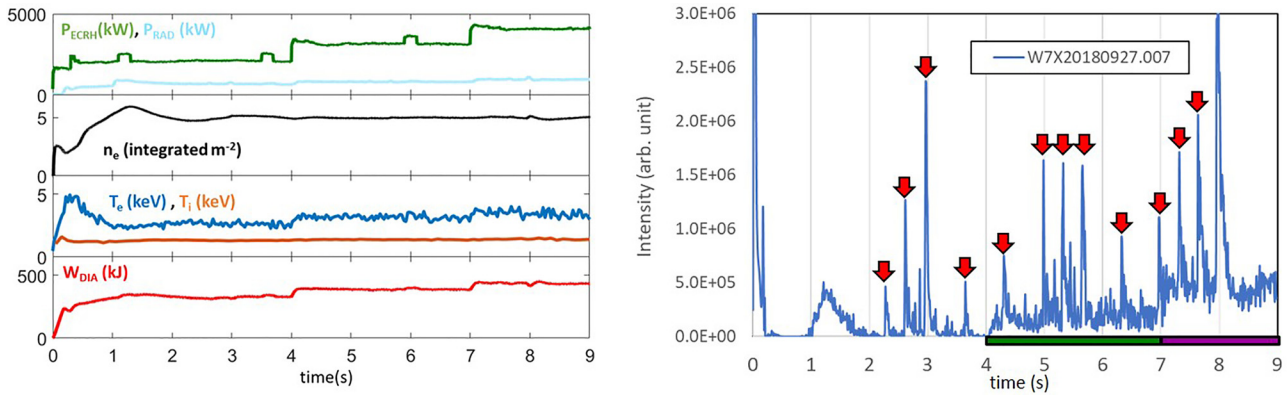

FIG. 8. Injection evaluation for W7-X experimental program 20180927-07. From top to bottom, the panels on the left show the injected power (PECRH), radiated power (PRAD), line integrated density (ne), electron and ion temperatures (Te, Ti), and the discharge stored energy (WDIA). The graph at right displays integrated pixel intensities from the EDICAM visible camera on port AEQ31. The confirmed PMPI injection events are denoted by the red arrows. The camera image is background subtracted with an early frame from the same discharge. An increase in ECRH heating from 2 to 3 MW at t = 4–7 s (green bar) and from 3 to 4 MW at t = 7–10 s (violet bar) are responsible for the increased baseline radiance during those periods and have been subtracted out accordingly for the final ascertainment of peak area used in injection quantification.

injections allowing some confidence in pulse to pulse and shot to shot comparisons. Another limitation on the accuracy of this conversion is the observation that for many injections, a substantial fraction of the illuminated pixels were saturated. As such, values obtained utilizing the conversion factor should be viewed as an approximate lower bound on injection quantity. The upper bound can be provided by the quantity of material conveyed by the powder feeder portion of the PMPI, understandable as the injector cannot disburse more material than is physically present. Thus, while this method of supplemental calibration is insufficient for a strict quantitative analysis of the injection driven events reported later in this work, it does provide a framework to allow an initial classification of the results.

Given the limitations of the camera based conversion factor, it is reasonable to question the value of this numeric over a simple application of the laboratory calibration. The need for supplemental calibration of the injection quantities was dictated by an observed strongly increasing level of material injection recorded during experimental program 20180927–47 as seen in the illumination history shown in the top panel of Fig. 9. For this discharge, the front of the PMPI was moved to major radius r = 6.13 m, which places it 5 cm from the island scrape off layer, and the piezoelectric vibration was set to produce approximately 40 mg/pulse in an effort to generate maximum particle entrainment. These settings resulted in a series of increasing injection amounts over the course of the discharge. This ramping of the injection quantity can be understood if one observes that there is a delay between the programmatic request for an increased powder injection rate, as was done for this discharge, and the full delivery of that rate as caused by the transit time for the thicker layer of powder to traverse the feeder tray and reach the impeller blades. As such the injection output is only anticipated to approach the calibrated PMPI output near the end of the injection series. Applying the previously arrived at a calibration factor, we can estimate the range of injected material deposited into the discharge to vary from ∼1 mg/pulse to over 30 mg/pulse with the possibility of injections reaching 60 mg/pulse. Panels (a)–(c) shown on the lower half of Fig. 9 display single frame camera images, which illustrate the variation in optical signature observed with different quantities of powder injection. In these images, the PMPI is located midway down the right hand side of the image. Here, we observe a rapid integration of material into the scrape off layer of the discharge, and for the largest injection, obvious entrainment of a radiative material into field aligned structures.

To further check this method, the spectroscopic boron-V signal at 4.857 nm provided by the HEXOS diagnostic was examined. The integrated injection peaks were compared to the initial pulse, and a relative injection quantity was determined. Again, assuming this initial

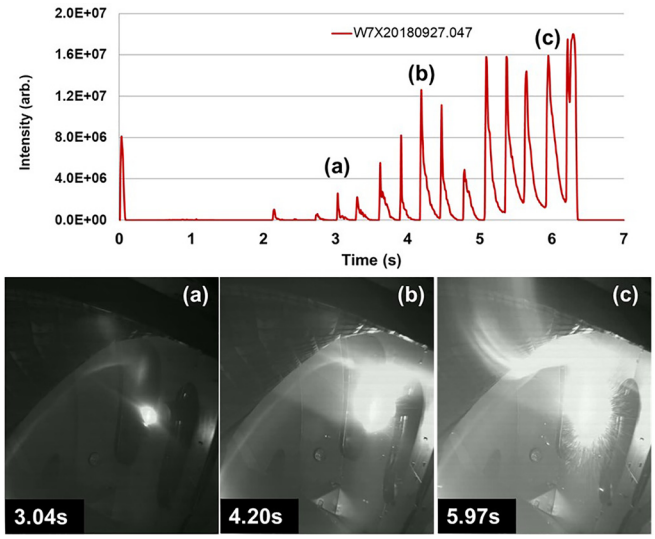

FIG. 9. Quantification of injection amount utilizing integral pixel intensity. The top graph displays the time history of injections from the W7-X experimental program 20180927-47. The bottom row of images shows the optical signatures observed for three separate injection events. Comparing optical signatures against a calibration factor derived during a previous discharge provides estimated quantities of injected material in the lower panels of 1–2 (a), 10–20 (b), and 30–60 mg (c), respectively.

injection consistent with laboratory calibrations and, thus, representative of approximately 1 mg/pulse as was found with the camera method, we find the relative intensities of the subsequent peaks to be largely in agreement with the survey camera method. The utilization of the survey camera method was chosen as the preferential method as the injected powder was observed to transit the interior of the vessel in both the clockwise and counterclockwise manners, and as the HEXOS diagnostic is a localized measurement 140° away from the injection site, there were concerns that variations in toroidal conductance and redeposition of material would add extra uncertainty to the measurement.

The summary of these conversions is given in Table I, which shows injection quantities estimated by QSV camera signals, relative injection quantities as determined by the HEXOS diagnostic, and the estimated range of injection quantities provided by these methods. We note again that we are not claiming a precise measurement of injection quantity and that the range that provides in the last table row represents the rough accuracy limits of this method. Injections in this discharge appear to fall into three categories as distinguished by both the estimated size of injection and their respective effects upon the discharge. The initial injections, prior to 4 s, are of quantities less than 10 mg per pulse and do not appear to strongly perturb the plasma. During the next period of injections from 4 to 5 s, injected quantities between 10 and 20 mg per pulse are observed and a transient positive effect upon the plasma is recorded, with that effect having concluded prior to the next injection. For the final period of injections from 5 to 6.5 s, injection quantities above 20 mg are estimated and the net beneficial effects upon the plasma, while varying, continue throughout the pulse sequence until the final pulse triggers a radiative collapse of the discharge at $t = 6.2$ s. Discussion of these injections and their subsequent effects upon the plasma will be covered in Sec. III C.

Overall these experiments have shown the W7-X discharges to be continually robust to material injection at quantities up to 20 mg/pulse or 60 mg/s. At these levels of externally applied heating (4 MW ECRH), the plasma is able to subsume and then expel the injected powder, returning to a baseline state prior to the next injection event as evidenced by only a marginal rise in Z_{eff}, to be shown in Sec. IV C. There are no indications that the plasma could not continue in this state for an extended period of time, suggesting that this level of material introduction could be utilized for future PFC conditioning studies. For injections larger than 20 mg/pulse, the plasma does not return to a baseline state between pulses and the continued injection of material leads to an impurity buildup and the expected radiative collapse for this discharge. We note that as a consequence of the rapid plasma termination at the end of the injection series, the full boron carbide load from the final injection pulse was not assimilated into the plasma. This resulted in a mobilization of an incompletely ablated material during the startup of the subsequent discharge and an additional radiative collapse. This effect was limited to the next discharge, and subsequent operations were conducted without noted deleterious effect from PMPI injections.

C. Injection effects on plasma behavior

Our discussion focuses on the results obtained during W7-X experimental program 20180927–47, and the overall behavior of them is shown in Fig. 10. While the effects noted here can be observed in the other B_4C injection experiments to a lesser extent, this was the

TABLE I. Estimation of injection quantities for experimental program 20180927-47. The top row indicates the start time of the pulse being analyzed, while the next two rows are the integrated pixel intensities from the QSV cameras and that conversion into approximate mg quantities. The quantities in the third row are the integrated HEXOS signal for the same pulses, while the fourth row is the relative injection quantity estimation arrived at by normalizing the initial pulse to 1 mg. Given the uncertainties in this measurement method, the final row represents the injection quantity range of the pulses, which we are utilizing for classification purposes.

Pulse start (s)	2.1	2.7	3.0	3.3	3.6	3.9	4.2	4.5	4.8	5.1	5.4	5.6	5.9	6.2
QSV pixel counts	3.9×10^6	2.7×10^6	7.6×10^6	1.2×10^7	2.8×10^7	2.0×10^7	6.6×10^7	4.6×10^7	3.6×10^7	1.0×10^8	1.0×10^8	1.1×10^8	1.3×10^8	1.9×10^8
Injection quantity QSV (mg)	0.9	0.6	1.8	2.9	6.7	4.7	15.7	10.9	8.5	23.7	24.6	25.3	31.3	45.3
HEXOS signal intensity	50		91	92	358	315	849	616	434	1151	1146	1154	1592	2712
Injection quantity HEXOS (mg)	1.0		1.8	1.8	7.1	6.3	16.9	12.2	8.6	22.8	22.8	22.9	31.6	53.9
Estimated injection quantity (mg/pulse)	1–10						10–20					20–60		

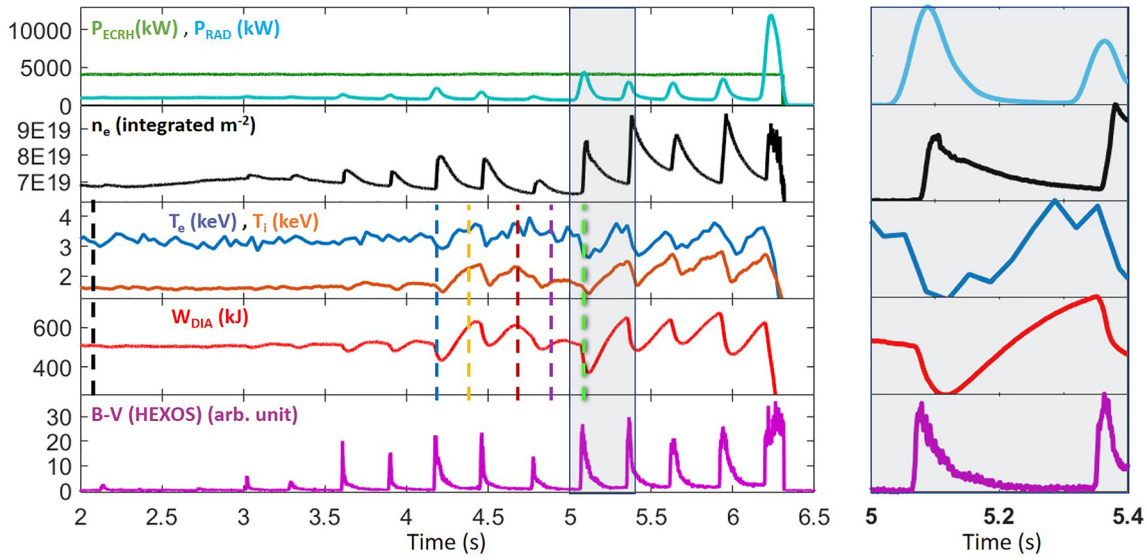

FIG. 10. Powder injection effects upon overall discharge behavior for experimental program 20180927-47. From top to bottom, the panels show the injected power (P_{ECRH}), radiated power (P_{RAD}), line integrated density (n_e), electron and ion temperatures (T_e, T_i), discharge stored energy (W_{DIA}), and the time evolution of the boron-V line as recorded by the HEXOS diagnostic. The dashed colored lines correspond to temperature and density profile slices displayed in Fig. 11. The gray box on the right shows a time expanded section of the respective traces corresponding to the box in the figure on the left.

only discharge subject to injections larger than 10 mg/pulse. In addition, the range in pulse sizes allows a direct comparison of the effects of multiple injection quantities on plasma behavior within the same discharge.

The smallest injections that occur in the period from 2.5 to 4 s produce mild transient increases in the radiated power and density, as observed in the top two panels of Fig. 10. These injections do not appear to result in substantial changes to either the core electron or ion temperature resolvable among the nominal signal variations and only result in minor depressions in the overall plasma stored energy. The perturbations to all signals return to a baseline level in the time between injection events. We also note that the ECRH probes do not report a significant reaction of non-absorbed power due to material injection, and thus, the absorbed ECRH power (P_{ECRH}) is nominally constant over the course of the experimental program.

The series of moderate injections from 4.1 to 5.2 s generate more substantial modifications to overall behavior and will be used to explore the demonstrated and repeatable effects upon the plasma. The radial profiles of the ion and electron temperatures as well as the electron density, at the times highlighted by the colored dashed lines in Fig. 10, are shown in Fig. 11. The dashed black trace corresponds to a pre-injection time of 2.08 s and is the baseline to which future profiles are compared. The profiles corresponding to times $t = 4.18$ s and $t = 5.08$ s are taken during the initial mass incursion phase of PMPI pulses. Upon injection into the plasma, the incident material is ablated by electrons rapidly free streaming along the field lines. Because of the long connection lengths present in the W7-X stellarator, these electrons draw energy from large sections of the edge plasma, thus rapidly equilibrating the temperature along the edge flux surfaces. The energy utilized for ionization in the edge causes core electron heat losses leading to the observed reduction in core electron temperature (T_e) seen in both the third panel of Fig. 10 and the blue and green profiles in panel (b) of Fig. 11. Also observed is a rise in the edge electron density (n_e, Fig. 11) and a loss of overall stored energy (W_{DIA}). The interplay of these effects for the injection at $t = 5.07$ s is highlighted by the expanded panel on the right of Fig. 10. Strong increases in the observed radiated power and spikes in the boron-V HEXOS[43] signal also occur in conjunction with the incorporation of the injected boron carbide into the plasma. For these moderate injections, we observe that the ion temperatures remain at baseline levels during the initial phase of the injection event.

Once the material is fully integrated into the plasma, the radiated power and boron signal intensity return to near baseline levels. For reasons we will explore in Sec. IV, during this post-injection phase as denoted by $t = 4.38$ and $t = 4.68$ traces in Fig. 11, there is a strong increase in the core ion temperature as well as a more moderate increase in the electron temperatures above the pre-injection level. The peak core ion temperatures are increased above the baseline temperatures by greater than 30% from a nominal value of 1.7 keV prior to granule injection to a maximum of 2.2–2.3 keV. The fact that the ion temperatures display a slower response to the injections indicates that the observed variations may themselves be a reaction to the previously enumerated changes in plasma parameters (n_e, T_e), rather than a direct consequence of material injection.

There is also a strong response exhibited by the stored energy (W_{DIA}, Fig. 10, fourth panel).[42] While the stored energy decreases promptly with the introduction of material, during the recovery phase it is observed to exceed the pre-injection value. Examining the expanded section on the right hand side of Fig. 10, we can see that approximately 100 ms after an injection event W_{DIA} has recovered to a pre-injection level. At this point, instead of remaining at the baseline level, it continues to increase for an additional 150 ms to a level up to

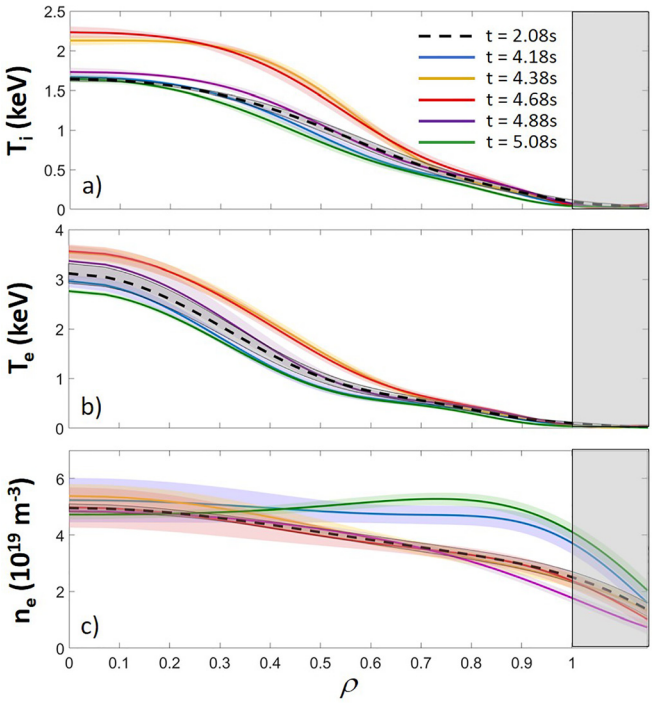

FIG. 11. Evolutions in plasma profiles for ion temperature (a), electron temperature (b), and electron density (c) as a result of boron carbide pulses between 4 s and 5.1 s during W7-X experimental program 20180927-47. Line colors in the above graphs correspond to colored bars in Fig. 10. Lines are fit to data from Thomson scattering (n_e and T_e) and x-ray imaging spectroscopy (XICS) (T_i) with error bands reflecting the scatter of the data. The gray area denotes radial locations outside the LCFS.

30% larger than the initial value. For moderate injections, this increase in the stored energy can then be seen to roll over and begin to decay back to the nominal discharge stored energy prior to the next injection event. The increase in the stored energy cannot be simply attributed to an increase in density as the expanded panels show the stored energy reaching a peak even as the density has returned to near nominal quantities. The profiles corresponding to t = 4.88 s display the plasma state observed just 50 ms after a more modest injection. As shown, the electron temperature is mildly raised; however, unlike traces from 150 ms after larger injections, there is not yet a corresponding strong rise in the core ion temperature.

Transitioning to the period of largest injections from 5 to 6.5 s, we note that in addition to the prompt responses, there are also sustained effects to the overall plasma behavior. In Fig. 12, we show the electron temperature and density profile responses to a series of injections. The black trace in the first panel is indicative of a pre-injection electron temperature profile taken at t = 2.08 s. The change from this profile to the one just after a pulsed powder injection can be seen in the difference between the red and black traces in panels (a) and (b). In panel (a), the red trace corresponding to a measurement at t = 5.08 s is taken just after the peak of an injection event. The exact timing of the pulse with respect to the measurement time can be seen in the HEXOS signal of the 4.85 nm B-V emission line at the bottom of the figure. Similar to the moderate size injections, there is a reduction in electron temperature as the injected material enters the discharge. The electron temperature remains depressed as the boron is assimilated into the discharge at t = 5.18 s trace, before rebounding to a level higher than the previous baseline level as t = 5.28 s trace with the core electron temperatures now observed at 3.5 keV as opposed to the 3.15 keV recorded before the series of injections began. In panel (b), the incoming pulse is observed to generate a profile with increased edge density as the material is absorbed. Note that when comparing the early injection time (red) to the baseline pre-injection levels (black), we see that there is no change in core density during the early injection time periods consistent with the outside-in absorption of material. The later time traces show a relaxation of the steep edge gradient as the material is transported into the core at t = 5.18 and t = 5.28 s. This evolution of the electron temperature is repeated in panels (c) and (e) for the two subsequent B_4C injections. Again we observe a suppressed core electron temperature as the material is injected and absorbed with a rebound of core performance once the boron has been fully integrated into the plasma.

Examining the three red traces in panels (b), (d), and (e) of Fig. 12, we observe the plasma relaxation from the induced flat profile as the material is assimilated. Density profile n_e [panel (b)] (t = 5.08 s) occurs 15 ms after the leading edge of the boron trace is recorded and is peaked at $\rho \approx 0.8$. The panel (d) density profile at t = 5.38 s, recorded 30 ms after the B-V leading edge, shows that the profile has now flattened. The third set of density profiles traces [panel (f)] begins with a trace at t = 5.68 s, which occurs 70 ms past the B-V leading edge. This profile shows a return to the standard peaked density profile as the edge has absorbed and either flushed or transmitted to the core; the majority of the boron pulse with just a remnant of the electron density are shown between the t = 5.68 s trace (red) and the other traces in the panel. In closely examining the behavior of the intermediate t = 5.78 s (green) trace, we also note that the density profile appears to relax to the baseline behavior also in an outside-in manner with the edge matching the late time profile before the profile at the center of the discharge responds.

Elevations of the ion temperature in response to large material injections exceed those of the moderate injections as previously discussed. As shown in 2D profile evolutions in Fig. 13, the moderate pulses prior to 5 s are capable of generating performance improvements, in some cases exceeding the empirical limit of 1.8 keV observed during the majority of W7-X discharges.[1] These improvements are transitory, lasting at most 250 ms, roughly the interval between pulses, prior to a return to the discharge baseline state. However, once the injection quantity becomes large (>20 mg) after t = 5 s, the plasma no longer completely returns to a baseline state between injections. Thus, while the peak ion temperature is reduced due to the subsequent injection, gains resulting from the previous injection are not completely diminished resulting in the core ion temperature being driven to a new peak height during each subsequent enhanced confinement phase. These evolutions are captured in the ion temperature profiles comprising panels (b)–(d) with the measurement time called out by the colored boxes on the bottom of the diamagnetic energy trace in panel (e). As a unique feature of this graph series, the final time trace in a previous panel (for example, t = 5.38 s) is repeated in the panel below to facilitate a better comparison between injection pulses. This feature illustrates that the ion temperature, which is elevated in an earlier pulse, serves as a basis from which the next pulse builds.

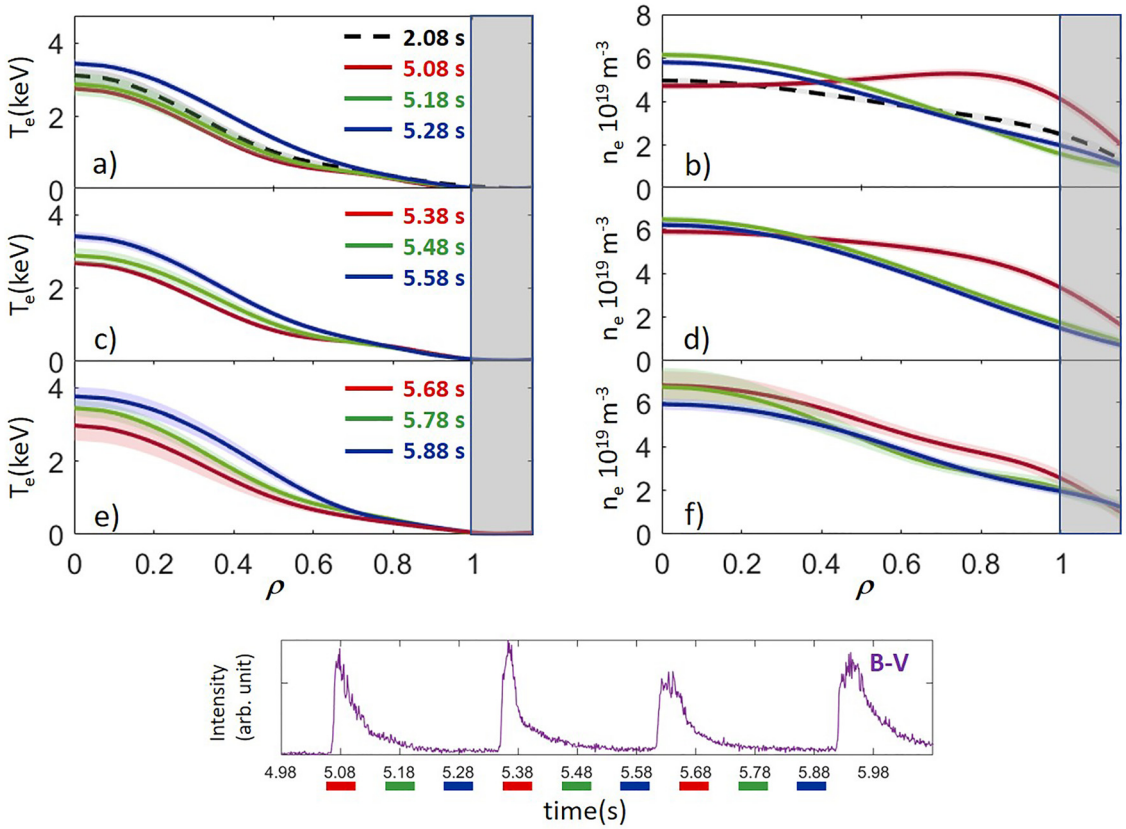

FIG. 12. Electron temperature and density responses to large quantity pulse injections for W7-X experimental program 20180927-47. The black dashed trace in panels (a) and (b) corresponds to a pre-injection measurement of electron temperature and density. The response to powder injection is shown with the red, green, and blue traces displaying fits to the early, middle, and late cycle responses, respectively. Panels (c) and (d) display similar traces for the second pulse shown in the HEXOS trace on the bottom, while panels (e) and (f) show traces for the third injection pulse. Gray panels correspond to areas outside the last confined flux surface.

The single slice ion temperature profile fits shown here are constrained by the electron temperature in the edge to remove the condition, whereby the ion temperature exceeds the electron temperature in these electron-only heated plasmas. The profiles are also flattened in the core to correct for elevated core temperature inversions due to low signal driven by the fast time resolution needed to resolve fine scale features. Thus, while the 2D trace of the inverted XICS data does display instances of the measured core T_i values greater than 3 keV, because of these constraints on the analyzed profile slices, we only claim a performance boost to 2.6 keV.

IV. DISCUSSION

During the majority of the standard ECRH powered discharges, which comprise the bulk of W7-X operations during OP1.1 and 1.2,[1,57] T_e was observed to be substantially larger than T_i with a flat core density profile and a generally positive core radial electric field indicating electron root confinement.[46,58] Noted in these experiments was the observation of an empirical limit to the core ion temperatures of approximately 1.8 keV suggesting anomalous loss mechanisms and transport roughly an order of magnitude larger than W7-X optimized neoclassical transport levels.[59,60] Within the present operational space, we expect that the three primary candidate modes, which could be responsible for the turbulent transport, are the Electron Temperature Gradient (ETG), Ion Temperature Gradient (ITG), and Trapped Electron Modes (TEMs).[61] Gyrokinetic simulations[62] have shown that the W7-X three dimensional geometry prevents significant transport from the electron scale ETG modes,[63] while the fact that the longitudinal invariant "J" displays a maximum value on the magnetic axis, the so-called maximum-J property[64] means that the trapped electrons are localized into regions of good curvature.[65] This leaves microinstabilities, driven by the presence of a strong ITG band, and unstable under normal W7-X operational conditions,[66,67] as a proposed mechanism to explain anomalous losses and, thus, the empirical limitation to core ion temperatures.

There are, however, some instances where the observed ion temperature limit has been exceeded. The most studied of these has been pellet enhanced discharges.[68–70] In the period following the injection of a stream of frozen hydrogen pellets into W7-X plasmas, an elevation of core ion temperatures above 3 keV is recorded, with overall energy confinement temporarily surmounting the ISS04 scaling. The improvement in transport is consistent with a stabilization of the previously enumerated ITG turbulence[71] as a result of strongly peaked density profiles caused by deep fueling from the pellet train injection. This temporary stabilization reduces anomalous transport and increases the overall plasma stored energy leading to a reversal of the

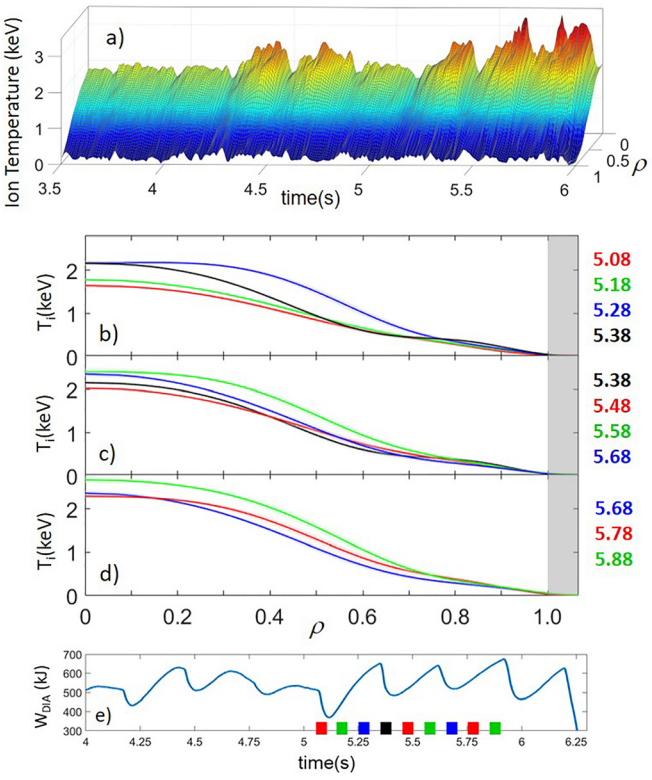

FIG. 13. Progression of ion temperature profiles in response to material injection during W7-X experimental program 20180927-47. Panel (a) displays the 2D evolution of the ion temperature in response to moderate and large injections. Ion temperatures within the core above 2 keV (yellow to red on the color scale) signify an elevation above those temperatures recorded in standard ECRH heated W7-X discharges. Panels (b)–(d) display radial profile response to PMPI injections. Note that the final time trace within panel (b) is repeated in panel (c) to allow evaluation of the continuing increase in core temperatures. Similarly, the final time trace within panel (c) is repeated in panel (d) for similar effect. The colored boxes on the x-axis of panel (e) show the respective state of the plasma diamagnetic energy during the profile evaluation times.

core radial electric field as the plasma transitions from electron to ion root.

These performance parameters are observed to be grossly similar to those observed during the post-injection phases of PMPI discharges and, thus, may suggest similar nascent causes. The effects of B_4C Injection into the W7-X plasma contain 2 distinct stages. The first stage is described by a change in the electron temperature and density profiles in response to the injection, while the second stage is characterized by the plasma response to these modified profiles and results in an increase in the ion temperature and overall discharge stored energy as well as confinement time. Having covered the first stage in Sec. III, we turn to the second stage of the injection event.

A. Modification of plasma gradients and turbulence suppression

The initiation of the enhanced confinement period starts with the evolution of the density profiles. The ablation and ionization of the newly introduced material leads to a substantial increase in edge electron density. For example, a 10 mg pulse contributes a localized influx of up to 4.4×10^{20} boron and 1.1×10^{20} carbon atoms if fully integrated into the plasma. These contributions effect not just the magnitude but also the shape of the resultant profiles. This can be seen in the modification of profile gradients displayed in left hand panels (a), (c), and (e) of Fig. 14. The major variations observed over the course of injection are to the density gradient. During the initial mass assimilation phase, the edge density for $\rho > 0.8$ is strongly steepened, which leads to a much flatter density throughout the core. However, once this phase has completed, the density gradient is steepened over the entire radial profile of the plasma. Periods of greatest enhanced confinement at $t = 5.28$ s also coincide with times of enhanced ion temperature gradients from $\rho = 0.8$ to $\rho = 0.4$. Experiments detailing enhanced performance of W7-X plasmas after pellet injection have also noted the most efficient turbulence stabilization to occur when steep density and temperature gradients are found to radially overlap[70] in support of the hypothesis of transiently stabilized ITG modes.

The changes in normalized inverse scale length, defined by $|a/L_{ne}| = a^*|\nabla_{\mathbf{r}}(n_e)|/n_e$, $|a/L_{Te}| = a^*|\nabla_{\mathbf{r}}(T_e)|/T_e$ and $|a/L_{Ti}| = a^*|\nabla_{\mathbf{r}}(T_i)|/T_i$ for minor radius $a = 0.5$ m, are shown in corresponding right hand side panels (b), (d), and (f) of Fig. 14. The strongly reduced gradient scale length during the injection phase moves the plasma deeper into the so-called stability valley,[64] which occurs at conditions unfavorable for ITG and TEM growth,[72] and this movement in turn drives a decrease in anomalous transport levels.

A consequence of this transition should be observable as a reduction in the presence of turbulent microstructures within the plasma. The measurement shown in Fig. 15 displays just such a reduction in the radially resolved density fluctuations during the post-powder injection periods (open markers) when compared to the pre-injection baseline (filled markers). This suggests a suppression of turbulence and, thus, a subsequent reduction in anomalous transport. We assert that following the recovery of the electron temperature, after the injected material has been ablated, ionized, and thermalized, this reduction in transport allows for an extended electron–ion collisional interaction time, which is most likely responsible for the observed higher ion temperatures given that the only heating for this plasma is delivered through ECRH.

B. Ambipolar electric field reversal and enhanced plasma confinement

The species specific radial flux that occurs within the stellarator geometry as a consequence of the ambipolarity condition[73] results in the neoclassical self-generation of a radial electric field. In the majority of W7-X ECRH heated plasmas, where $T_e \gg T_i$, this results in a positive radial electric field in the plasma core and the observation therein of the so-called electron-root confinement.[46] However, during the enhanced confinement periods observed in PMPI discharges, the gap between core electron and ion temperature drops from 1.4 keV before injection to a minimum of 500 eV primarily due to an increase in ion temperature. As a consequence of these increased ion temperatures, there is an observed reversal of the radial electric field corresponding to the "ion-root" solution of the ambipolarity relation[74] as displayed in Fig. 16. In panel (a), the radial electric field as measured by the XICS is observed to be positive in the plasma core during the period before injection and has transitioned to a negative electric field as recorded

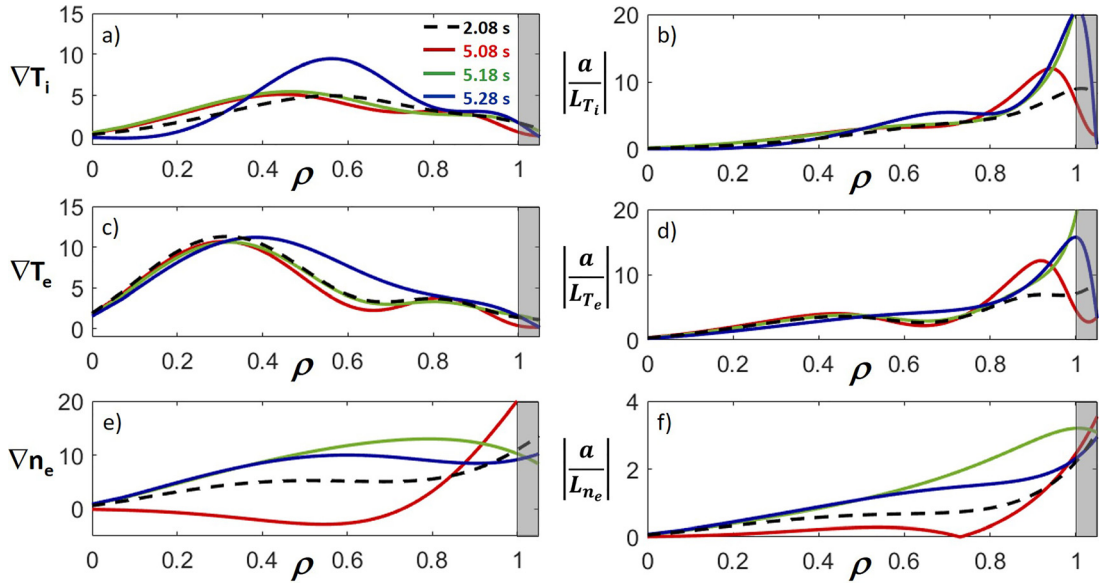

FIG. 14. Record of gradient and scale length changes in response to powder injection in W7-X experimental program 20180927-47. The graphs at left represented by panels (a), (c), and (e) show, respectively, the changes in ion temperature, election temperature, and electron density gradients both prior to the injection series (t = 2.08 s) and in response to the injection, which occurred at approximately t = 5.07 s. The panels on the right (b), (d), and (f), respectively, show the response of the inverse gradient scale length for the same period and quantities. The gray boxes represent the area past the LCFS.

after assimilation of the injected material. Examining the time history of the electric field as shown in panel (b) clear indications of core ion root confinement occur coincident with the instances of enhanced performance. This measurement of the radial electric field is corroborated by a similar results recorded by the Doppler Reflectometer (DR). As with the XICS, a measurement of the perpendicular rotation velocity is utilized to determine the electric field and the result is displayed panel (c) of Fig. 16. As is shown, the radial electric field during periods of post-injection enhanced confinement is more strongly negative than is observed during the periods prior to injection. Note that values presented in the figure are normalized by $E_r/\nabla r$ from the recorded data to account for the flux surface compression at the bean shaped outboard midplane location of the Doppler Reflectometer. Examining the XICS and DR traces, we note that similar normalized radii for the two measurements are in generally good agreement in shape and in value to within a factor of 2. For example, the primary negative peak of the DR measurement at rho = 0.6 is coincident with a strong negative swing of the XICS measurement at this value prior to the error bars of the XICS becoming large due to the lack of highly ionized argon in these outer radii. Similarly, the pre-injection values for the XICS and DR are slightly negative and essentially flat from rho = 0.6 to rho = 0.3. The positive swing evidenced by the XICS in the core region of the plasma is not resolved in this measurement by the DR.

The projected neoclassical ambipolar radial electric field can be calculated by solving the drift kinetic equation for a given set of temperature and density profiles. A comparison of this with the XICS radial electric field measurement as done in Ref. 48 shows good agreement over a significant portion of the W7-X operational space. To compare current measurements with theory, a neoclassical calculation of the electric field utilizing the SFINCS (Stellarator Fokker–Planck Iterative Neoclassical Conservative Solver[75]) code. For these calculations, the ion temperature measurements from the XICS diagnostic as well as the electron temperature and density measurements from Thomson scattering are used as inputs to generate a numerical solution of the drift-kinetic equation for the species specific distribution function generating neoclassical fluxes and flows. The results of the electric field portion of the calculation, as displayed in panel (d) of Fig. 16, show that the depression of the electric field in response to the modified electron and ion temperature and density profiles is consistent with the underpinnings of neoclassical theory. While this calculation and the corresponding two measurements do not match exactly [note the difference in vertical scale between panel (a) and panels (c) and (d)], there is good general agreement on the ability of the powder injection and the resulting changes in plasma profiles to significantly modify the radial electric field.

In these experiments, both E_r and E_r-shear may have an impact in the stabilization of density fluctuations. As shown in Fig. 15 and panel (c) of Fig. 16, the reduction in the density fluctuations is measured in the radial range where the E_r-shear increases (rho $\approx$ 0.4–0.9), which points to the stabilizing effect of the E_r-shear as a relevant player. This effect, however, does not exclude the stabilizing effect of the E_r itself that can be relevant particularly in stellarators. This has been shown in Ref. 71, where the impact of the E_r on turbulence was studied using the gyrokinetic code GENE for W7-X configuration. These simulations show how E_r produces a displacement of the fluctuations in the magnetic surface toward regions with lower curvature less favorable for turbulence generation with the subsequent reduction in the turbulent transport.

Further evaluation of neoclassical energy flux in both the electron and ion root phases shows an amplified ion energy flux during periods of ion-root confinement significant enough that ions become the dominant neoclassical loss channel.[48] This is also consistent with a

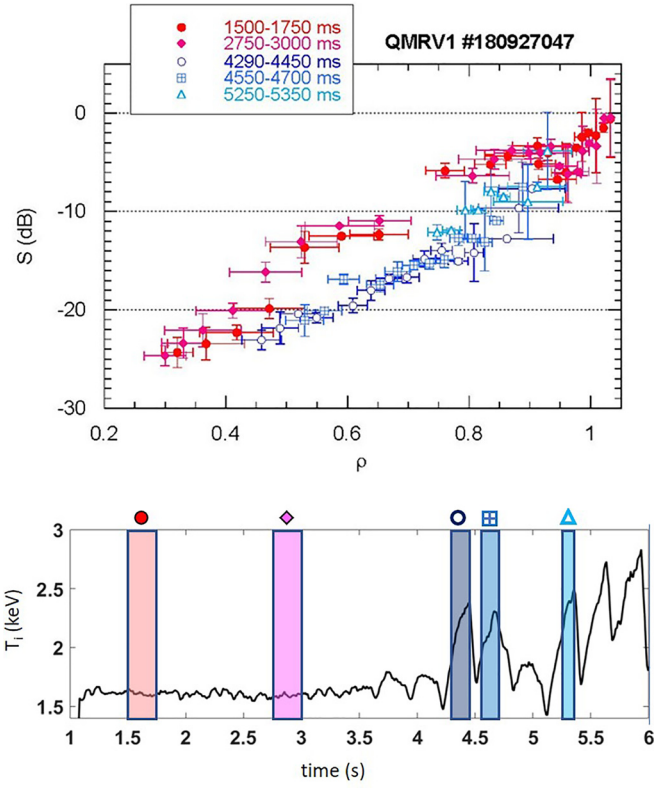

FIG. 15. Doppler reflectometry measurement of radially resolved density fluctuations during W7-X experimental program 20180927-47. Solid markers in the top panel denote pre-injection measurements, while hollow markers are indicative of post-injection enhanced confinement periods. The bottom panel shows core ion temperature as measured by XICS. The colored bands denote time intervals for the respective period of measurement.

reduction in anomalous losses from turbulent transport and manifests as a transient increase in the stored energy. Given that the input ECRH power was maintained at a constant level over the course of the injection series this indicated a period of enhanced confinement. An average confinement time of 130 ms is observed during the pre-injection period from 1 to 2 s as shown in Fig. 17. While this value then oscillates in response to the injections, the experimental energy confinement time, $\tau_E^{exp} = W_{dia}/(P_{ECRH} - dW_{dia}/dt)$, can be seen to reach values of 210 ms during periods of enhanced confinement. These periods are also notable as they clearly surmount the value predicted by the ISS04 empirical scaling also shown in the figure. We note here that as the ISS04 scaling is intended as a metric for performance of stationary plasma conditions, a strict comparison to the transient elevations of the PMPI discharge is not completely tractable. However, given that the periods of enhanced confinement are on the order of a confinement time and, thus, could be considered quasi-stationary, we offer the comparison as a figure of merit.

C. Additional Observations

As to be expected, the introduction of increasing levels of B_4C impurities generated a marked change in the effective ion charge (Z_{eff}). As shown in Fig. 18, small injections (<10 mg) have little impact with impurity flushing completed in the interval between pulses allowing the plasma to return to a baseline state. The effective ion charge increases from approximately 1.3 at the beginning of the discharge to an elevated secondary plateau near 2 during the period of medium injection quantities from 4 to 5 s. For injections larger than 20 mg/pulse, the Z_{eff} measurement continues to increase with each subsequent pulse reaching an average of 3.5 with oscillations due to impurity injections and their subsequent flushing. It is only through repeated pulses of increasing magnitude that we reach a point whereby the discharge is no longer able to support the impurity burden at the present input power and the discharge suffers a radiative collapse.

The primary impurity species within the discharge; boron, carbon, and oxygen, respectively, are shown in the three lower panels, highlighting inter-pulse variations and changes in the overall baseline level. The given signal values are based on a Simpson integration over the line peaks with a local linear background subtraction. As such, signal levels cannot be compared between any two lines, but each line shows the correct run of its individual signal level with the influence of neighboring lines reduced by the local background subtraction. There is a general increase in the boron signal as the injection quantity increases with the stepwise increase in a direct consequence of periodic injections from the PMPI and the inability of the discharge to completely flush that quantity of impurities prior to the next pulse. However, we note that there is no corresponding increase in the carbon baseline level, which is concomitantly introduced as a component of the boron carbide molecule. This may be due to the fact that while PMPI injections are the primary contributor of B into these plasmas, the local graphite tiles provide a substantially larger C source than is generated by injections. While only the carbon V line intensity is displayed, similar behavior has been noted over the ionization species from C-II to C-VI. Contrasting these signals is the observed decrease in overall oxygen signal intensity once the pulsed impurity injections begin, as shown in the bottom trace, the oxygen level at the end of the pulse sequence is roughly half of the pre-injection intensity level. This overall behavior is observed with varying degrees in the ionization species from O-III through O-VI but with minimal response from the O-VII signal.

As PMPI experiments were also intended to provide a first estimation of the efficacy of an Impurity Powder Dropper as an alternate means of wall conditioning for W7-X, spectroscopic data were scrutinized for evidence of wall conditioning. The expectations to generate conditioning effects were low due to the sustained discharge improvements observed by W7-X as a result of the standard boronizations. The observation that plasma improvements resulting from a gaseous boronization did not appear to significantly degrade during experimental operations conducted between the three boronizations could indicate that there was still an effective deposition layer on the plasma facing component. This would then mitigate any observable impact from additional material deposition. As such it was unsurprising that an attempt to determine a positive impact on wall conditioning as directly provided by the PMPI was inconclusive. At this juncture, all that can be stated with certainty is that the operation of the PMPI did not have a deleterious impact on the overall wall condition or on subsequent experiments during OP1.2b. Absent the installation of a full IPD system, an adequate assessment of the powder injection effects by the PMPI on wall conditioning might best be accomplished by a

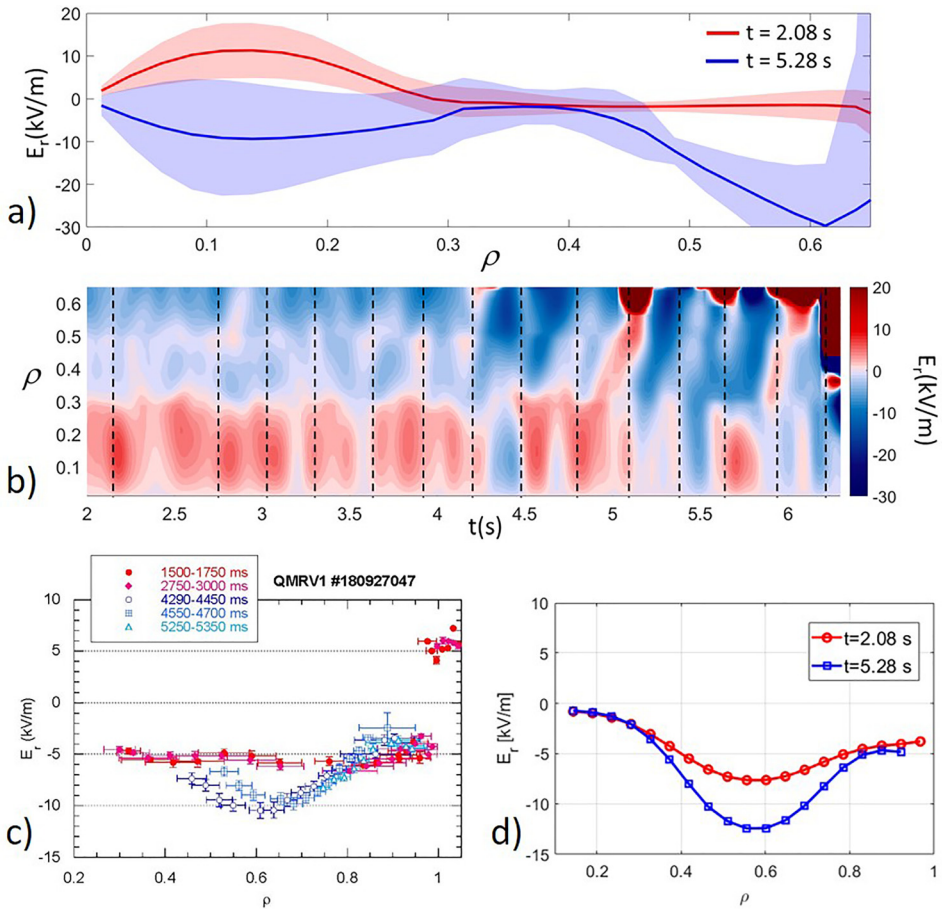

FIG. 16. Electric field response to injection events in W7-X experimental program 20180927-47. Panel (a) displays the ambipolar radial electric field as measured by XICS for a period prior to and during the injection event along with the corresponding shaded error bands. As indicated by the increasing size of the error band, XICS measurements at normalized radii greater than $\rho = 0.6$ are not well constrained during the injection series. Panel (b) shows the radial electric field evolution over the course of the discharge with dotted lines overlayed to indicate the pulse start times. Measurements in panel (c) are provided by doppler reflectometry. The red filled markers denote the electric field for times prior to particle injection while the blue hollow markers are a measurement of post-injection electric field. Panel (d) displays a SFINCS neoclassical calculation of the ambipolar radial electric field with the red circles representing the calculated field prior to injection while the blue squares denote the post-injection field.

dedicated set of PMPI experiments in either an unboronized machine or one far from a standard boronization.

In addition, we also note that the high material fluence experiments were only attempted in the standard 5/5 magnetic configuration. In this configuration, a flux tube followed along any of the five topologically distinct individual magnetic islands will return to its original location after a single toroidal transit. Replicating the PMPI experiments in both high (5/4) and low iota (5/6) rotational transform configurations might lead to greater contact between the initial injection site and a variety of plasma facing surfaces as these magnetic geometries are comprised of a single island chain transiting the vessel multiple times before returning to its original location. These configurations provide an extended connection length between the injection location and a plasma facing surface,[26] and thus, the impurity loaded island chain would have greater access to a range of limiter and divertor surfaces. These configurations and respective changes in material transport as a result of the altered magnetic field could be an interesting aspect of future experiments and would also allow correlation to recent results from full torus modeling of IPD boron injections at LHD[76] and DIII-D,[77] which predicted asymmetries in the SOL impurity density accumulation and emission as well as material deposition.

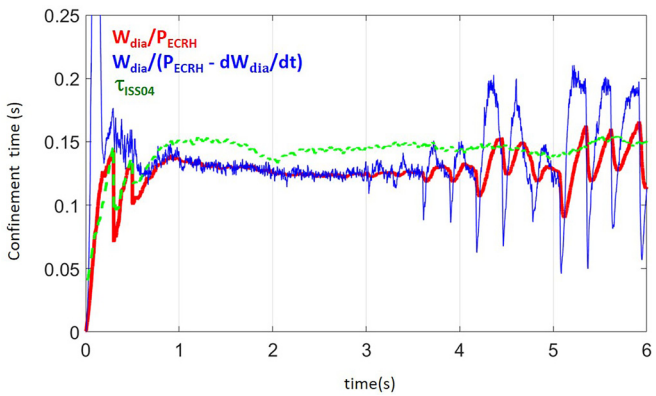

FIG. 17. Comparison of confinement time scaling. The confinement time for W7-X experimental program 20180927-47 is calculated, both with and without the variations in stored energy being taken into account as shown by the red and blue traces, respectively. This is compared to the instantaneous ISS04 scaling for the given set of plasma parameters.

V. SUMMARY

The PMPI was successfully tested during the recent W7-X operation campaign with a demonstrated ability to inject on demand boron carbide pulses displaying good particle entrainment and unexpected effects on overall discharge behavior. Particles were horizontally injected at a range of pulse injection quantities from less than 1 mg up

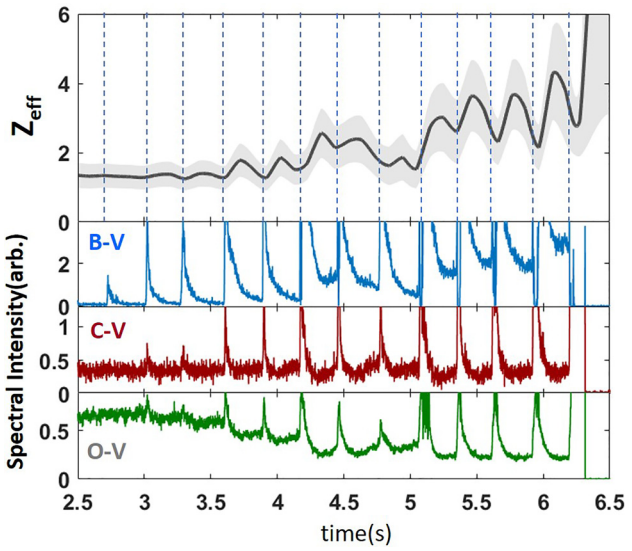

FIG. 18. Evolution of effective ion charge and impurity concentration during the injection series in W7-X experimental program 20180927-47. Periodic variations of Z_{eff} in response to injections can be seen in the top panel with the colored band representing standard deviation error in the measurement and the dotted lines denoting pulse injection start times. The bottom panels focus on spectroscopic evolution of the interpulse impurity level for the common impurities boron, carbon, and oxygen.

to at least 30 mg as determined by an *in situ* measurement of local ablation characteristics. Wide angle cameras show rapid ablation of the injected particles and entrainment of impurity loads into field aligned flux tubes transiting the vessel. Observations of carbon filtered divertor imaging show direct engagement of injected material with high flux plasma facing surfaces allowing for the possibility of depositional coating. This, coupled with the observation that deposited boron tends to migrate around the vessel during normal plasma operation,[1] provides support for the utilization of a single source of particulate injection to effectively distribute material throughout the vacuum vessel. In addition, by providing an array of injection events we are able to demonstrate a sustainable impurity burden for present W7-X experimental programs providing a baseline for future conditioning efforts.

Injected impurities are observed to enter the confined region of the discharge as evidenced by an increase in overall radiated power as well as increases in plasma density and measured Z_{eff}. Prompt response to injection also includes a reduction in electron temperature, a decrease in stored energy, and an increase in spectroscopic boron intensity as the injected material is absorbed and thermalized. However, once the estimated injection quantity exceeds approximately 10 mg/pulse, there are more substantial effects upon the plasma behavior. Once the material has been assimilated into the discharge, there is an observed increase in the ion temperature and stored energy. For moderate injection sizes, the duration of these effects is contained to the times between the individual pulses and so does not appear to generate cumulative effects, whereas the larger injections (<20 mg) generate a sustained increase in the core ion temperature. The accompanying increase in stored energy also continues to trend upward until the point where it is abruptly terminated by the subsequent introduction of an additional pulse of boron carbide, leading to radiative collapse.

The presumed sequence of events leading to these enhanced confinement periods proceeds as follows. The injection of the boron carbide powder depresses the electron temperature and shifts the location of density gradient. While unconfirmed during PMPI injection discharges, gyrokinetic simulations[71] of turbulence reduction via electron density peaking are supportive of the postulate that these conditions lead to a reduction in the anomalous transport, thus providing an extended time for electron–ion temperature equilibration resulting in increased ion temperatures. The reduction in temperature gap between the electrons and ions is then responsible for the reversal of the ambipolar electric field, transitioning the core of the plasma from an electron root to ion root confinement, which in turn provides greater confinement and stored energy. A subsequent burst of powder eliminates this enhanced confinement by rapidly exhausting energy through the electron channel during material ablation. As such no definitive statement can be made about the expected lifetime of the enhanced confinement mode. It is assumed that the enhanced confinement will degrade as the density gradient decays leading to a return of greater anomalous transport and a loss of high temperature ions returning the ambipolar electric field to its nominal ECRH driven state.

In conclusion, we assert that systematic experiments with the PMPI could help to determine whether the utilization of a powder dropper as a real time conditioning technique would support the W7-X goals by assisting in the maintenance of premium wall conditions over the course of extreme long pulse (20 min+) discharges. Given the strong, but transient enhanced performance metrics generated during boron carbide injection discharges, we also believe that a more thorough investigation of these parameters could be a strong candidate for future investigation. As such, the ability of particle injection to maintain premium wall conditioning and possibly aid in plasma performance through profile shaping could certainly be viewed as a cooperative asset in future W7-X high performance long pulse campaigns.

ACKNOWLEDGMENTS

This research was supported by the U.S. DOE under Contract No. DE-AC02-09CH11466 with Princeton University. This work has been carried out within the framework of the EUROfusion Consortium and has received funding from the Euratom research and training programme 2014–2018 and 2019–2020 under Grant Agreement No. 633053. The views and opinions expressed herein do not necessarily reflect those of the European Commission.

DATA AVAILABILITY

The data that support the findings of this study are available from the corresponding author upon reasonable request.

REFERENCES

[1]T. Klinger, T. Andreeva, S. Bozhenkov, C. Brandt, R. Burhenn, B. Buttenschön, G. Fuchert, B. Geiger, O. Grulke, H. P. Laqua, N. Pablant *et al.*, "Overview of first W7X high performance operation," Nucl. Fusion **59**, 112004 (2019).
[2]J. Huang, X. Gong, A. M. Garofalo, J. Qian, J. Chen, M. Wu, M. Li, Q. Yuan, L. Wang, C. Pan, X. Lin, Q. Yang, A. Ekedahl, R. Maingi, C. T. Holcomb, E. Li,

L. Zeng, B. Zhang, J. F. Chang, X. J. Zhang, M. Goniche, Y. Peysson, X. Zhu, Y. Sun, G. Xu, Q. Zang, L. Zhang, H. Liu, B. Lyu, R. Ding, Q. Ren, B. Ding, W. Guo, S. Ding, N. Xiang, Y. Liang, F. Liu, Y. Zhao, B. Xiao, J. Hu, C. Hu, L. Hu, X. Gao, P. Fu, Y. Song, X. D. Zhang, V. Chan, J. Li, B. Wan, and EAST Team, "Progress of physics understanding for long pulse high-performance plasma on EAST towards the steady state operation of ITER and CFETR," Nucl. Fusion **62**, 014019 (2020).

[3]H. K. Park, M. J. Choi, S. H. Hong, Y. In, Y. M. Jeon, J. S. Ko, W. H. Ko, J. G. Kwak, J. M. Kwon, J. Lee, J. H. Lee, W. Lee, Y. B. Nam, Y. K. Oh, B. H. Park, J. K. Park, Y. S. Park, S. J. Wang, M. Yoo, S. W. Yoon, J. G. Bak, C. S. Chang, W. H. Choe, Y. Chu, J. Chung, N. Eidietis, H. S. Han, S. H. Hahn, H. G. Jhang, J. W. Juhn, J. H. Kim, K. Kim, A. Loarte, H. H. Lee, K. C. Lee, D. Mueller, Y. S. Na, Y. U. Nam, G. Y. Park, K. R. Park, R. A. Pitts, S. A. Sabbagh, G. S. Yun, and KSTAR Team, "Overview of KSTAR research progress and future plans toward ITER and K-DEMO," Nucl. Fusion **59**, 112020 (2019).

[4]Y. Yoshimura, H. Kasahara, M. Tokitani, R. Sakamoto, Y. Ueda, S. Ito, K. Okada, S. Kubo, T. Shimozuma, H. Igami, H. Takahashi, T. I. Tsujimura, R. Makino, S. Kobayashi, Y. Mizuno, T. Akiyama, N. Ashikawa, S. Masuzaki, G. Motojima, M. Shoji, C. Suzuki, H. Tanaka, K. Tanaka, T. Tokuzawa, H. Tsuchiya, I. Yamada, Y. Goto, H. Yamada, T. Mutoh, A. Komori, Y. Takeiri, and LHD Experiment Group, "Progress of long pulse discharges by ECH in LHD," Nucl. Fusion **56**, 046005 (2016).

[5]C. Bourdelle, J. F. Artaud, V. Basiuk, M. Bécoulet, S. Brémond, J. Bucalossi, H. Bufferand, G. Ciraolo, L. Colas, Y. Corre, X. Courtois, J. Decker, L. Delpech, P. Devynck, G. Dif-Pradalier, R. P. Doerner, D. Douai, R. Dumont, A. Ekedahl, N. Fedorczak, C. Fenzi, M. Firdaouss, J. Garcia, P. Ghendrih, C. Gil, G. Giruzzi, M. Goniche, C. Grisolia, A. Grosman, D. Guilhem, R. Guirlet, J. Gunn, P. Hennequin, J. Hillairet, T. Hoang, F. Imbeaux, I. Ivanova-Stanik, E. Joffrin, A. Kallenbach, J. Linke, T. Loarer, P. Lotte, P. Maget, Y. Marandet, M. L. Mayoral, O. Meyer, M. Missirlian, P. Mollard, P. Monier-Garbet, P. Moreau, E. Nardon, B. Pégourié, Y. Peysson, R. Sabot, F. Saint-Laurent, M. Schneider, J. M. Travère, E. Tsitrone, S. Vartanian, L. Vermare, M. Yoshida, R. Zagorski, and JET Contributors, "WEST physics basis," Nucl. Fusion **55**, 063017 (2015).

[6]T. Härtl, A. Drenik, M. Kircher, V. Rohde, F. Stelzer, W. Zeidner, and ASDEX Upgrade Team, "Optimization of the ASDEX Upgrade glow discharge," Fusion Eng. Des. **124**, 283–286 (2017).

[7]T. Wauters, D. Borodin, R. Brakel, S. Brezinsek, K. J. Brunner, J. Buermans, S. Coda, A. Dinklage, D. Douai, O. Ford, G. Fuchert, A. Goriaev, H. Grote, A. Hakola, E. Joffrin, J. Knauer, T. Loarer, H. Laqua, A. Lyssoivan, V. Moiseenko, D. Moseev, J. Ongena, K. Rahbarnia, D. Ricci, V. Rohde, S. Romanelli, S. Sereda, T. Stange, F. L. Tabarés, L. Vanó, O. Volzke, E. Wang, ASDEX Upgrade Team, TCV Team, EUROfusion MST1 Team, W7-X Team, JT-60SA Team, and JET Contributors, "Wall conditioning in fusion devices with superconducting coils," Plasma Phys. Controlled Fusion **62**, 034002 (2020).

[8]V. Rohde, R. Dux, A. Kallenbach, K. Krieger, and R. Neu, and ASDEX Upgrade Team, "Wall conditioning in ASDEX Upgrade," J. Nucl. Mater. **363–365**, 1369–1374 (2007).

[9]R. Brakel, A. Dinklage, J. Fellinger, G. Fuchert, H. Grote, R. König, H. Laqua, T. Stange, O. Volzke, G. Schlisio, U. Wenzel, D. Zhang, A. Goriaev, T. Wauters, S. Brezinsek, V. Moiseenko, and A. A. Belitskii, "Strategy and optimisation of wall conditioning at the Wendelstein 7-X stellarator," in *IAEA Fusion Energy Conference* Gandhinagar, India, IAEA, 22–27 October, 2018, Paper No. IAEA-CN-258/EX/P8-17; available at https://nucleus.iaea.org/sites/fusionportal/Shared%20Documents/FEC%202018/fec2018-preprints/preprint0231.pdf.

[10]A. Nagy, A. Bortolon, D. M. Mauzey, E. Wolfe, E. P. Gilson, R. Lunsford, R. Maingi, D. K. Mansfield, R. Nazikian, and A. L. Roquemore, "A multi-species powder dropper for magnetic fusion applications," Rev. Sci. Instrum. **89**(10), 10K121 (2018).

[11]H. W. Kugel, M. G. Bell, H. Schneider, J. P. Allain, R. E. Bell, R. Kaita, J. Kallman, S. Kaye, B. P. LeBlanca, D. Mansfield, R. E. Nygren, R. Maingi, J. Menard, D. Mueller, M. Ono, S. Paul, S. Gerhardt, R. Raman, S. Sabbagh, C. H. Skinner, V. Soukhanovskii, J. Timberlake, L. E. Zakharov, and NSTX Research Team, "Lithium coatings on NSTX plasma facing components and its effects on boundary control, core plasma performance, and operation," Fusion Eng. Des. **85**(6), 865–873 (2010).

[12]R. Maingi, J. S. Hu, Z. Sun, K. Tritz, G. Z. Zuo, W. Xu, M. Huang, X. C. Meng, J. M. Canik, A. Diallo, R. Lunsford, D. K. Mansfield, T. H. Osborne, X. Z. Gong, Y. F. Wang, Y. Y. Li, and EAST Team, "ELM elimination with Li powder injection in EAST discharges using the tungsten upper divertor," Nucl. Fusion **58**, 024003 (2018).

[13]Z. Sun, A. Diallo, R. Maingi, Y. Z. Qian, K. Tritz, Y. F. Wang, Y. M. Wang, A. Bortolon, A. Nagy, L. Zhang, Y. M. Duan, Y. Ye, H. L. Zhao, H. Q. Wang, X. Gu, G. Z. Zuo, W. Xu, M. Huang, C. L. Li, X. C. Meng, C. Zhou, H. Q. Liu, Q. Zang, L. Wang, J. P. Qian, G. S. Xu, X. Z. Gong, J. S. Hu, and EAST Team, "Suppression of edge localized modes with real-time boron injection using the tungsten divertor in EAST," Nucl. Fusion **61**, 014002 (2021).

[14]E. P. Gilson, H. H. Lee, A. Bortolon, A. Diallo, S. H. Hong, R. Maingi, D. Mansfield, A. Nagy, S. H. Park, S. W. Yoon, W. H. Choe, and R. Nazikian, "Wall conditioning and ELM mitigation with boron nitride powder injection in KSTAR," Nucl. Mater. Energy **28**, 101043 (2021).

[15]F. Nespoli, N. Ashikawa, E. P. Gilson, R. Lunsford, S. Masuzaki, M. Shoji, T. Oishi, C. Suzuki, A. Nagy, A. Mollen, N. A. Pablant, K. Idab, M. Yoshinuma, N. Tamura, D. A. Gates, T. Morisaki, and LHD Experiment Group, "First impurity powder injection experiments in LHD," Nucl. Mater. Energy **25**, 100842 (2020).

[16]A. Bortolon, V. Rohde, R. Maingi, E. Wolfrum, R. Dux, A. Herrmann, R. Lunsford, R. M. McDermott, A. Nagy, A. Kallenbach, D. K. Mansfield, R. Nazikian, R. Neu, and ASDEX Upgrade Team, "Real-time wall conditioning by controlled injection of boron and boron nitride powder in full tungsten wall ASDEX Upgrade," Nucl. Mater. Energy **19**, 384–389 (2019).

[17]A. Bortolon, R. Maingi, A. Nagy, J. Ren, J. D. Duran, A. Maan, D. C. Donovan, J. A. Boedo, D. L. Rudakov, A. W. Hyatt, T. W. Wilks, M. W. Shafer, C. M. Samuell, M. E. Fenstermacher, E. P. Gilson, R. Lunsford, D. K. Mansfield, T. Abrams, and R. Nazikian, "Observations of wall conditioning by means of boron powder injection in DIII-D H-mode plasmas," Nucl. Fusion **60**, 126010 (2020).

[18]R. Maingi, D. P. Boyle, J. M. Canik, S. M. Kaye, C. H. Skinner, J. P. Allain, M. G. Bell, R. E. Bell, S. P. Gerhardt, T. K. Gray, M. A. Jaworski, R. Kaita, H. W. Kugel, B. P. LeBlanc, J. Manickam, D. K. Mansfield, J. E. Menard, T. H. Osborne, R. Raman, A. L. Roquemore, S. A. Sabbagh, P. B. Snyder, and V. A. Soukhanovskii, "The effect of progressively increasing lithium coatings on plasma discharge characteristics, transport, edge profiles and ELM stability in the National Spherical Torus Experiment," Nucl. Fusion **52**, 083001 (2012).

[19]Z. Sun, R. Maingi, J. S. Hu, W. Xu, G. Z. Zuo, Y. W. Yu, C. R. Wu, M. Huang, X. C. Meng, L. Zhang, L. Wang, S. T. Mao, F. Ding, D. K. Mansfield, J. Canik, R. Lunsford, A. Bortolon, X. Z. Gong, and EAST Team, "Real time wall conditioning with lithium powder injection in long pulse H-mode plasmas in EAST with tungsten divertor," Nucl. Mater. Energy **19**, 124–130 (2019).

[20]R. Lunsford, V. Rohde, A. Bortolon, R. Dux, A. Herrmann, A. Kallenbach, R. M. McDermott, P. David, A. Drenik, F. Laggner, R. Maingi, D. K. Mansfield, A. Nagy, R. Neu, E. Wolfrum, and ASDEX Upgrade Team, "Active conditioning of ASDEX Upgrade tungsten plasma-facing components and discharge enhancement through boron and boron nitride particulate injection," Nucl. Fusion **59**, 126034 (2019).

[21]T. Wauters, A. Goriaev, A. Alonso, J. Baldzuhn, R. Brakel, S. Brezinsek, A. Dinklage, H. Grote, J. Fellinger, O. P. Ford, R. König, H. Laqua, D. Matveev, T. Stange, L. Vanód, and W7-X Team, "Wall conditioning throughout the first carbon divertor campaign on Wendelstein 7-X," Nucl. Mater. Energy **17**, 235–241 (2018).

[22]A. Goriaev, T. Wauters, R. Brakel, S. Brezinsek, A. Dinklage, J. Fellinger, H. Grote, D. Moseev, S. Sereda, O. Volzke, and W7-X Team, "Wall conditioning at the Wendelstein 7-X stellarator operating with a graphite divertor," Phys. Scr. **2020**, 014063.

[23]S. Sereda, S. Brezinsek, E. Wang, T. Barbui, R. Brakel, B. Buttenschön, A. Goriaev, U. Hergenhahn, U. Höfel, M. Jakubowski, A. Knieps, R. König, M. Krychowiak, S. Kwak, Y. Liang, D. Naujoks, A. Pavone, M. Rasinski, L. Rudischhauser, M. Ślęczka, J. Svensson, H. Viebke, T. Wauters, Y. Wei, V. Winters, D. Zhang, and W7-X Team, "Impact of boronizations on impurity sources and performance in Wendelstein 7-X," Nucl. Fusion **60**, 086007 (2020).

[24]A. Nagy, A. Bortolon, D. Gates, E. Gilson, C. Killer, T. Klinger, R. Lunsford, R. Maingi, D. Mansfield, D. Mauzey, R. Nazikian, L. Roquemore, and E. Wolfe, "A horizontal powder injector for W7X," Fusion Eng. Des. **146**, 1403–1407 (2019).

[25]D. Nicolai, V. Borsuk, P. Drews, O. Grulke, K. P. Hollfeld, T. Krings, Y. Liang, C. Linsmeier, O. Neubauer, G. Satheeswaran, B. Schweer, G. Offermanns, and W7-X Team, "A multi-purpose manipulator system for W7-X as user facility for plasma edge investigation," Fusion Eng. Des. **123**, 960–964 (2017).
[26]C. Killer, O. Grulke, P. Drews, Y. Gao, M. Jakubowski, A. Knieps, D. Nicolai, H. Niemann, A. P. Sitjes, G. Satheeswaran, and W7-X Team, "Characterization of the W7-X scrape off layer using reciprocating probes," Nucl. Fusion **59**, 086013 (2019).
[27]R. Lunsford, A. Bortolon, A. L. Roquemore, D. K. Mansfield, M. A. Jaworski, R. Kaita, R. Maingi, and A. Nagy, "Multi-species impurity granule injection and mass deposition projections in NSTX-U discharges," Nucl. Fusion **57**, 076008 (2017).
[28]R. Lunsford, A. Bortolon, R. Maingi, D. K. Mansfield, A. Nagy, G. L. Jackson, and T. Osborne, "Supplemental ELM control in ITER through beryllium granule injection," Nucl. Mater. Energy **19**, 34–41 (2019).
[29]C. Beidler, G. Grieger, F. Herrnegger, E. Harmeyer, J. Kisslinger, W. Lotz, H. Maassberg, P. Merkel, J. Nührenberg, F. Rau, J. Sapper, F. Sardei, R. Scardovelli, A. Schlüter, and H. Wobig, "Physics and engineering design for Wendelstein VII-X," Fusion Sci. Tech. **17**, 148–168 (1990).
[30]A. Dinklage, C. D. Beidler, P. Helander, G. Fuchert, H. Maaßberg, K. Rahbarnia, T. Sunn Pedersen, Y. Turkin, R. C. Wolf, A. Alonso, T. Andreeva, B. Blackwell, S. Bozhenkov, B. Buttenschön, A. Czarnecka, F. Effenberg, Y. Feng, J. Geiger, M. Hirsch, U. Höfel, M. Jakubowski, T. Klinger, J. Knauer, G. Kocsis, A. Krämer-Flecken, M. Kubkowska, A. Langenberg, H. P. Laqua, N. Marushchenko, A. Mollén, U. Neuner, H. Niemann, E. Pasch, N. Pablant, L. Rudischhauser, H. M. Smith, O. Schmitz, T. Stange, T. Szepesi, G. Weir, T. Windisch, G. A. Wurden, D. Zhang, and W7-X Team, "Magnetic configuration effects on the Wendelstein 7-X stellarator," Nat. Phys. **14**, 855–860 (2018).
[31]Y. Feng, F. Sardei, J. Kisslinger, P. Grigull, K. McCormick, and D. Reiter, "3D edge modeling and island divertor physics," Contrib. Plasma Phys. **44**, 57–69 (2004).
[32]S. A. Lazerson, S. Bozhenkov, B. Israeli, M. Otte, H. Niemann, V. Bykov, M. Endler, T. Andreeva, A. Ali, P. Drewelow, M. Jakubowski, A. P. Sitjes, F. Pisano, B. Cannas, and W7-X Team, "Error fields in the Wendelstein 7-X stellarator," Plasma Phys. Controlled Fusion **60**(12), 124002 (2018).
[33]S. A. Lazerson, Y. Gao, K. Hammond, C. Killer, G. Schlisio, M. Otte, C. Biedermann, M. Spolaore, S. Bozhenkov, J. Geiger, O. Grulke, D. Nicolai, G. Satheeswaran, H. Niemann, M. Jakubowski, P. Drewelow, A. P. Sitjes, A. Ali, B. Cannas, F. Pisano, R. König, G. Wurden, G. Kocsis, T. Szepesi, U. Wenzel, M. Mulsow, K. Rahbarnia, J. Schilling, U. Neuner, T. Andreeva, H. Thomsen, J. Knauer, K. J. Brunner, B. Blackwell, M. Endler, S. Klose, L. Rudischhauser, and W7-X Team, "Tuning of the rotational transform in Wendelstein 7-X," Nucl. Fusion **59**(12), 126004 (2019).
[34]T. S. Pedersen, R. König, M. Krychowiak, M. Jakubowski, J. Baldzuhn, S. Bozhenkov, G. Fuchert, A. Langenberg, H. Niemann, D. Zhang, K. Rahbarnia, H.-S. Bosch, Y. Kazakov, S. Brezinsek, Y. Gao, N. Pablant, and W7-X Team, "First results from divertor operation in Wendelstein 7-X," Plasma Phys. Controlled Fusion **61**, 014035 (2019).
[35]R. C. Wolf, A. Alonso, S. Äkäslompolo, J. Baldzuhn, M. Beurskens, C. D. Beidler, C. Biedermann, H.-S. Bosch, S. Bozhenkov, R. Brakel, H. Braune, S. Brezinsek, K.-J. Brunner, H. Damm, A. Dinklage, P. Drewelow, F. Effenberg, Y. Feng, O. Ford, G. Fuchert, Y. Gao, J. Geiger, O. Grulke, N. Harder, D. Hartmann, P. Helander, B. Heinemann, M. Hirsch, U. Höfel, C. Hopf, K. Ida, M. Isobe, M. W. Jakubowski, Y. O. Kazakov, C. Killer, T. Klinger, J. Knauer, R. König, M. Krychowiak, A. Langenberg, H. P. Laqua, S. Lazerson, P. McNeely, S. Marsen, N. Marushchenko, R. Nocentini, K. Ogawa, G. Orozco, M. Osakabe, M. Otte, N. Pablant, E. Pasch, A. Pavone, M. Porkolab, A. Puig Sitjes, K. Rahbarnia, R. Riedl, N. Rust, E. Scott, J. Schilling, R. Schroeder, T. Stange, A. von Stechow, E. Strumberger, T. Sunn Pedersen, J. Svensson, H. Thomson, Y. Turkin, L. Vano, T. Wauters, G. Wurden, M. Yoshinuma, M. Zanini, D. Zhang, and Wendelstein 7-X Team, "Performance of Wendelstein 7-X stellarator plasmas during the first divertor operation phase," Phys. Plasmas **26**, 082504 (2019).
[36]F. Effenberg, H. Niemann, Y. Feng, J. Geiger, O. Schmitz, Y. Suzuki, A. Ali, T. Barbui, S. Brezinsek, H. Frerichs, M. Jakubowski, R. Konig, M. Krychowiak, A. Puig Sitjes, J. C. Schmitt, T. S. Pedersen, and W7-X Team, "Investigation of 3D effects on heat fluxes in performance-optimized island divertor configurations at Wendelstein 7-X," Nucl. Mater. Energy **18**, 262–267 (2019).
[37]G. J. M. Hagelaar, D. Kogut, D. Douai, and R. A. Pitts, "Modelling of tokamak glow discharge cleaning I: Physical principles," Plasma Phys. Controlled Fusion **57**(2), 025008 (2014).
[38]A. Goriaev, T. Wauters, R. Brakel, H. Grote, M. Gruca, O. Volzke, S. Brezinsek, A. Dinklage, M. Kubkowska, and U. Neuner, "Development of glow discharge and electron cyclotron resonance heating conditioning on W7-X," Nucl. Mater. Energy **18**, 227–232 (2019).
[39]S. A. Bozhenkov, M. Beurskens, A. D. Molin, G. Fuchert, E. Pasch, M. R. Stoneking, M. Hirsch, U. Höfel, J. Knauer, J. Svensson, H. Trimiño Mora, and R. C. Wolf, "The Thomson scattering diagnostic at Wendelstein 7-X and its performance in the first operation phase," J. Instrum. **12**, P10004 (2017).
[40]E. Pasch, M. N. A. Beurskens, S. A. Bozhenkov, G. Fuchert, J. Knauer, R. C. Wolf, and W7-X Team, "The Thomson scattering system at Wendelstein 7-X," Rev. Sci. Instrum. **87**, 11E729 (2016).
[41]K. J. Brunner, T. Akiyama, M. Hirsch, J. Knauer, P. Kornejew, B. Kursinski, H. Laqua, J. Meineke, H. Trimiño Mora, and R. C. Wolfl, "Real-time dispersion interferometry for density feedback in fusion devices," J. Instrum. **13**, P09002 (2018).
[42]K. Rahbarnia, H. Thomsen, U. Neuner, J. Schilling, J. Geiger, G. Fuchert, T. Andreeva, M. Endler, D. Hathiramani, T. Bluhm, M. Zilker, B. B. Carvalho, A. Werner, and Wendelstein 7-X Team, "Diamagnetic energy measurements during the first operational phase at the Wendelstein 7-X stellarator," Nucl. Fusion **58**, 096010 (2018).
[43]B. Buttenschön, R. Burhenn, M. Kubkowska, A. Czarnecka, T. Fornal, N. Krawczyk, D. Zhang, N. Pablant, A. Langenberg, P. Valson, H. Thomsen, W. Biel, J. Aßmann, t Wendelstein, and 7-X. team, "Spectroscopic impurity survey in the first operation phase of Wendelstein 7-X," in *Proceedings of 43rd EPS Conference on Controlled Fusion and Plasma Physics*, Leuven, Belgium, European Physics Society, 2016, Vol. 40A, p. P4.012; available at http://ocs.ciemat.es/EPS2016PAP/pdf/P4.012.pdf.
[44]D. Hathiramani, A. Ali, G. Anda, T. Barbui, C. Biedermann, A. Charl, D. Chauvin, G. Czymek, C. P. Dhard, P. Drewelow, A. Dudek, F. Effenberg, G. Ehrke, M. Endler, D. A. Ennis, J. Fellinger, O. Ford, S. Freundt, D. Gradic, K. Grosser, J. Harris, H. Hölbe, M. W. Jakubowski, M. Knaup, G. Kocsis, R. König, M. Krause, T. Kremeyer, P. Kornejew, M. Krychowiak, H. T. Lambertz, H. Jenzsch, M. Mayer, S. Mohr, O. Neubauer, M. Otte, V. Perseo, D. Pilopp, L. Rudischhauser, O. Schmitz, B. Schweer, M. Schülke, L. Stephey, T. Szepesi, A. Terra, M. Toth, U. Wenzel, G. A. Wurden, S. Zoletnik, T. S. Pedersen, and W7-X Team, "Upgrades of edge, divertor and scrape-off layer diagnostics of W7-X for OP1.2," Fusion Eng. Des. **136**, 304–308 (2018).
[45]R. König, J. Baldzuhn, W. Biel, C. Biedermann, H. S. Bosch, S. Bozhenkov, T. Bräuer, B. Brotas de Carvalho, R. Burhenn, B. Buttenschön, G. Cseh, A. Czarnecka, M. Endler, V. Erckmann, T. Estrada, J. Geiger, O. Grulke, D. Hartmann, D. Hathiramani, M. Hirsch, S. Jabłonski, M. Jakubowski, J. Kaczmarczyk, T. Klinger, S. Klose, G. Kocsis, P. Kornejew, A. Krämer-Flecken, T. Kremeyer, M. Krychowiak, M. Kubkowska, A. Langenberg, H. P. Laqua, M. Laux, Y. Liang, A. Lorenz, A. O. Marchuk, V. Moncada, O. Neubauer, U. Neuner, J. W. Oosterbeek, M. Otte, N. Pablant, E. Pasch, T. S. Pedersen, K. Rahbarnia, L. Ryc, O. Schmitz, W. Schneider, H. Schuhmacher, B. Schweer, T. Stange, H. Thomsen, J.-M. Travere, T. Szepesi, U. Wenzel, A. Werner, B. Wiegel, T. Windisch, R. Wolf, G. A. Wurden, D. Zhang, A. Zimbal, S. Zoletnik, and W7-X Team, "The set of diagnostics for the first operation campaign of the Wendelstein 7-X stellarator," J. Instrum. **10**, P10002 (2015).
[46]N. A. Pablant, A. Langenberg, A. Alonso, C. D. Beidler, M. Bitter, S. Bozhenkov, R. Burhenn, M. Beurskens, L. Delgado-Aparicio, A. Dinklage, G. Fuchert, D. Gates, J. Geiger, K. W. Hill, U. Höfel, M. Hirsch, J. Knauer, A. Krämer-Flecken, M. Landreman, S. Lazerson, H. Maaßberg, O. Marchuk, S. Massidda, G. H. Neilson, E. Pasch, S. Satake, J. Svennson, P. Traverso, Y. Turkin, P. Valson, J. L. Velasco, G. Weir, T. Windisch, R. C. Wolf, M. Yokoyama, D. Zhang, and W7-X Team, "Core electric field and transport in Wendelstein 7-X plasmas," Phys. Plasmas **25**, 022508 (2018).
[47]N. A. Pablant, A. Langenberg, J. A. Alonso, M. Bitter, S. A. Bozhenkov, O. P. Ford, K. W. Hill, J. Kring, O. Marchuck, J. Svensson, P. Traverso, T. Windisch, Y. Yakusevitch, and W7-X Team, "Correction and verification of x-ray imaging

crystal spectrometer analysis on Wendelstein 7-X through X-ray ray tracing," Rev. Sci. Instrum. **92**, 043530 (2021).
[48]N. Pablant, A. Langenberg, A. Alonso, J. Baldzuhn, C. D. Beidler, S. Bozhenkov, R. Burhenn, K. J. Brunner, A. Dinklage, G. Fuchert, O. Ford, D. A. Gates, J. Geiger, M. Hirsch, U. Höfel, Y. O. Kazakov, J. Knauer, M. Krychowiak, H. Laqua, M. Landreman, S. Lazerson, H. Maaßberg, O. Marchuck, A. Mollen, E. Pasch, A. Pavone, S. Satake, T. Schröder, H. M. Smith, J. Svensson, P. Traverso, Y. Turkin, J. L. Velasco, A. von Stechow, F. Warmer, G. Weir, R. C. Wolf, D. Zhang, and W7-X Team, "Investigation of the neoclassical ambipolar electric field in ion-root plasmas on W7-X," Nucl. Fusion **60**, 036021 (2020).
[49]M. Hirsch, E. Holzhauer, J. Baldzuhn, B. Kurzan, and B. Scott, "Doppler reflectometry for the investigation of propagating density perturbations," Phys. Plasma Confined Fusion **43**, 1641 (2001).
[50]M. Hirsch, E. Holzhauer, and H.-J. Hartfuss, "Reflectometry for Wendelstein 7-X," Nucl. Fusion **46**, 5853 (2006).
[51]P. Hennequin, C. Honoré, A. Truc, A. Quéméneur, N. Lemoine, J.-M. Chareau, and R. Sabot, "Doppler backscattering system for measuring fluctuations and their perpendicular velocity on Tore Supra," Rev Sci. Instrum. **75**, 3881 (2004).
[52]G. D. Conway, J. Schirmer, S. Klenge, W. Suttrop, E. Holzhauer, and ASDEX Upgrade Team, "Plasma rotation profile measurements using Doppler reflectometry," Plasma Phys. Controlled Fusion **46**, 951 (2004).
[53]T. Happel, T. Estrada, E. Blanco, V. Tribaldos, A. Cappa, and A. Bustos, "Doppler reflectometer system in the stellarator TJ-II," Rev Sci. Instrum. **80**, 073502 (2009).
[54]D. Carralero, T. Estrada, T. Windisch, J. L. Velasco, J. A. Alonso, M. Beurskens, S. Bozhenkov, H. Damm, G. Fuchert, Y. Gao, M. Jakubowski, H. Nieman, N. Pablant, E. Pasch, G. Weir, and Wendelstein 7-X Team, "Characterization of the radial electric field and edge velocity shear in Wendelstein 7-X," Nucl. Fusion **60**, 106019 (2020).
[55]T. Estrada, D. Carralero, T. Windisch, E. Sanchez, J. M. García Regaña, J. Martínez, A. d l. Peña, J. L. Velasco, J. A. Alonso, M. N. A. Beurskens, S. A. Bozhenkov, H. Damm, G. Fuchert, R. Kleiber, N. A. Pablant, and E. Pasch, "Radial electric field and density fluctuations measured by Doppler reflectometry during the post-pellet enhanced confinement phase in W7-X," Nucl. Fusion **61**, 046008 (2021).
[56]G. Kocsis, T. Baross, C. Biedermann, G. Bodnár, G. Cseh, T. Ilkei, R. König, M. Otte, T. Szabolics, T. Szepesi, and S. Zoletnik, "Overview video diagnostics for the W7-X stellarator," Fusion Eng. Des. **96–97**, 808–811 (2015).
[57]R. C. Wolf, A. Ali, A. Alonso, J. Baldzuhn, C. Beidler, M. Beurskens, C. Biedermann, H.-S. Bosch, S. Bozhenkov, R. Brakel, A. Dinklage, Y. Feng, G. Fuchert, J. Geiger *et al.*, "Major results from the first plasma campaign of the Wendelstein 7-X stellarator," Nucl Fusion **57**, 102020 (2017).
[58]M. Hirsch, A. Dinklage, A. Alonso, G. Fuchert, S. Bozhenkov, U. Höfel, T. Andreeva, J. Baldzuhn, M. Beurskens, H.-S. Bosch, C. D. Beidler, C. Biedermann, E. Blanco *et al.*, "Confinement in Wendelstein 7-X limiter plasmas," Nucl. Fusion **57**, 086010 (2017).
[59]A. Langenberg, N. A. Pablant, T. Wegner, P. Traverso, O. Marchuk, T. Bräuer, B. Geiger, G. Fuchert, S. Bozhenkov, E. Pasch, O. Grulke, F. Kunkel, C. Killer, D. Nicolai, G. Satheeswaran, K. P. Hollfeld, B. Schweer, T. Krings, P. Drews, G. Offermanns, A. Pavone, J. Svensson, J. A. Alonso, R. Burhenn, R. C. Wolf, and W7-X Team, "Prospectus of X-ray imaging spectrometers for impurity transport: Recent results from the stellarator Wendelstein 7-X," Rev. Sci. Instrum. **89**, 10G101 (2018).
[60]B. Geiger, T. Wegner, C. D. Beidler, R. Burhenn, B. Buttenschön, R. Dux, A. Langenberg, N. A. Pablant, T. Pütterich, Y. Turkin, T. Windisch, V. Winters, M. Beurskens, C. Biedermann, K. J. Brunner, G. Cseh, H. Damm, F. Effenberg, G. Fuchert, O. Grulke, J. H. Harris, C. Killer, J. Knauer, G. Kocsis, A. Krämer-Flecken, T. Kremeyer, M. Krychowiak, O. Marchuk, D. Nicolai, K. Rahbarnia, G. Satheeswaran, J. Schilling, O. Schmitz, T. Schröder, T. Szepesi, H. Thomsen, H. Trimino Mora, P. Traverso, D. Zhang, and W7-X Team, "Observation of anomalous impurity transport during low density experiments in W7-X with laser blow-off injections of iron," Nucl. Fusion **59**, 046009 (2019).
[61]Av Stechow, O. Grulke, T. Wegner, J. H. E. Proll, J. A. Alcusón, H. M. Smith, J. Baldzuhn, C. D. Beidler, M. N. A. Beurskens, S. A. Bozhenkov, E. Edlund, B. Geiger, Z. Huang, O. P. Ford, G. Fuchert, A. Langenberg, N. Pablant, E. Pasch, M. Porkolab, K. Rahbarnia, J. Schilling, E. R. Scott, H. Thomsen, L. Vanó, G. Weir, and W7-X Team, "Suppression of core turbulence by profile shaping in Wendelstein 7-X," arXiv:2010.02160.
[62]G. G. Plunk, P. Xanthopoulos, G. M. Weir, S. A. Bozhenkov, A. Dinklage, G. Fuchert, J. Geiger, M. Hirsch, U. Hoefel, M. Jakubowski, A. Langenberg, N. Pablant, E. Pasch, T. Stange, D. Zhang, and W7-X Team, "Stellarators resist turbulent transport on the electron Larmor scale," Phys. Rev. Lett. **122**, 035002 (2019).
[63]J. M. Garcia-Regaña, M. Barnes, I. Calvo, F. I. Parra, J. A. Alcusón, R. Davies, A. González-Jerez, A. Mollén, E. Sánchez, J. L. Velasco, and A. Zocco, "Turbulent impurity transport simulations in Wendelstein 7-X plasmas," J. Plasma Phys. **87**, 855870103 (2021).
[64]J. A. Alcusón, P. Xanthopoulos, G. G. Plunk, P. Helander, F. Wilms, Y. Turkin, A. v Stechow, and O. Grulke, "Suppression of electrostatic instabilities in maximum J stellarators," Plasma Phys. Controlled Fusion **62**, 035005 (2020).
[65]P. Helander, J. H. E. Proll, and G. G. Plunk, "Collisionless microinstabilities in stellarators. I. Analytical theory of trapped-particle modes," Phys. Plasmas **20**, 122505 (2013).
[66]P. Helander, T. Bird, F. Jenko, R. Kleiber, G. G. Plunk, J. H. E. Proll, J. Riemann, and P. Xanthopoulos, "Advances in stellarator gyrokinetics," Nucl. Fusion **55**, 053030 (2015).
[67]E. J. Doyle, W. A. Houlberg, Y. Kamada, V. Mukhovatov, T. H. Osborne, A. Polevoi, G. Bateman, J. W. Connor, J. G. Cordey, T. Fujita, X. Garbet, T. S. Hahm, L. D. Horton, A. E. Hubbard, F. Imbeaux, F. Jenko, J. E. Kinsey, Y. Kishimoto, J. Li, T. C. Luce, Y. Martin, M. Ossipenko, V. Parail, A. Peeters, T. L. Rhodes, J. E. Rice, C. M. Roach, V. Rozhansky, F. Ryter, G. Saibene, R. Sartori, A. C. C. Sips, J. A. Snipes, M. Sugihara, E. J. Synakowski, H. Takenaga, T. Takizuka, K. Thomsen, M. R. Wade, H. R. Wilson, ITPA Transport Physics Topical Group, ITPA Confinement Database and Modelling Topical Group, and ITPA Pedestal and Edge Topical Group, "Plasma confinement and transport," Nucl. Fusion **47**, S18 (2007).
[68]J. Baldzuhn, H. Damm, C. D. Beidler, K. McCarthy, N. Panadero, C. Biedermann, S. A. Bozhenkov, K. J. Brunner, G. Fuchert, Y. Kazakov, M. Beurskens, M. Dibon, J. Geiger, O. Grulke, U. Höfel, T. Klinger, F. Köchl, J. Knauer, G. Kocsis, P. Kornejew, P. T. Lang, A. Langenberg, H. Laqua, N. A. Pablant, E. Pasch, T. S. Pedersen, B. Ploeckl, K. Rahbarnia, G. Schlisio, E. R. Scott, T. Stange, A. von Stechow, T. Szepesi, Y. Turkin, F. Wagner, V. Winters, G. Wurden, D. Zhang, and Wendelstein 7-X Team, "Pellet fueling experiments in Wendelstein 7-X," Plasma Phys. Controlled Fusion **61**, 095012 (2019).
[69]S. A. Bozhenkov, Y. Kazakov, O. P. Ford, M. N. A. Beurskens, J. Alcusón, J. A. Alonso, J. Baldzuhn, C. Brandt, K. J. Brunner, H. Damm, G. Fuchert, J. Geiger, O. Grulke, M. Hirsch, U. Höfel, Z. Huang, J. Knauer, M. Krychowiak, A. Langenberg, H. P. Laqua, S. Lazerson, N. B. Marushchenko, D. Moseev, M. Otte, N. Pablant, E. Pasch, A. Pavone, J. H. E. Proll, K. Rahbarnia, E. R. Scott, H. M. Smith, T. Stange, A. von Stechow, H. Thomsen, Y. Turkin, G. Wurden, P. Xanthopoulos, D. Zhang, R. C. Wolf, and W7-X Team, "High-performance plasmas after pellet injections in Wendelstein 7-X," Nucl. Fusion **60**, 066011 (2020).
[70]J. Baldzuhn, H. Damm, C. D. Beidler, K. McCarthy, N. Panadero, C. Biedermann, S. A. Bozhenkov, A. Dinklage, K. J. Brunner, G. Fuchert, Y. Kazakov, M. Beurskens, M. Dibon, J. Geiger, O. Grulke, U. Höfel, T. Klinger, F. Köchl, J. Knauer, G. Kocsis, P. Kornejew, P. T. Lang, A. Langenberg, H. Laqua, N. A. Pablant, E. Pasch, T. S. Pedersen, B. Ploeckl, K. Rahbarnia, G. Schlisio, E. R. Scott, T. Stange, A. V. Stechow, T. Szepesi, Y. Turkin, F. Wagner, V. Winters, G. Wurden, D. Zhang, and Wendelstein 7-X Team, "Enhanced energy confinement after series of pellets in Wendelstein 7-X," Plasma Phys. Controlled Fusion **62**, 05512 (2020).
[71]P. Xanthopoulos, S. A. Bozhenkov, M. N. Beurskens, H. M. Smith, G. G. Plunk, P. Helander, C. D. Beidler, J. A. Alcusón, A. Alonso, A. Dinklage, O. Ford, G. Fuchert, J. Geiger, J. H. E. Proll, M. J. Pueschel, Y. Turkin, F. Warmer, and W7-X Team, "Turbulence mechanisms of enhanced performance stellarator plasmas," Phys. Rev. Lett. **125**, 075001 (2020).
[72]M. Romanelli, C. R. Frascati, C. Bourdelle, and W. Dorland, "Effects of high density peaking and high collisionality on the stabilization of the electrostatic

turbulence in the Frascati Tokamak Upgrade," Phys. Plasmas **11**, 3845 (2004).
[73]S. P. Hirshman, K. C. Shaing, W. I. van Rij, C. O. Beasley, Jr., and E. C. Crume, Jr., "Plasma transport coefficients for nonsymmetric toroidal confinement systems," Phys. Fluids. **29**, 2951 (1986).
[74]D. E. Hastings, W. A. Houlberg, and K. C. Shaing, "The ambipolar electric field in stellarators," Nucl. Fusion **25**, 445 (1985).
[75]M. Landreman, H. M. Smith, A. Mollén, and P. Helander, "Comparison of particle trajectories and collision operators for collisional transport in nonaxisymmetric plasmas," Phys. Plasmas **21**, 042503 (2014).
[76]M. Shoji, G. Kawamura, R. Smirnov, Y. Tanaka, S. Masuzaki, Y. Uesugi, N. Ashikawa, E. Gilson, and R. Lunsford, "Full torus impurity transport simulation for optimizing plasma discharge operation using a multi-species impurity powder dropper in the large helical device," Contrib. Plasma. Phys. **60**, e201900101 (2019).
[77]F. Effenberg, A. Bortolon, H. Frerichs, B. Grierson, J. D. Lore, T. Abrams, T. E. Evans, Y. Feng, R. Lunsford, R. Maingi, A. Nagy, R. Nazikian, D. Orlov, J. Ren, D. L. Rudakov, W. R. Wampler, and H. Q. Wang, "3D modeling of boron transport in DIII-D L-mode wall conditioning experiments," Nucl. Mater. Energy **26**, 100900 (2021).